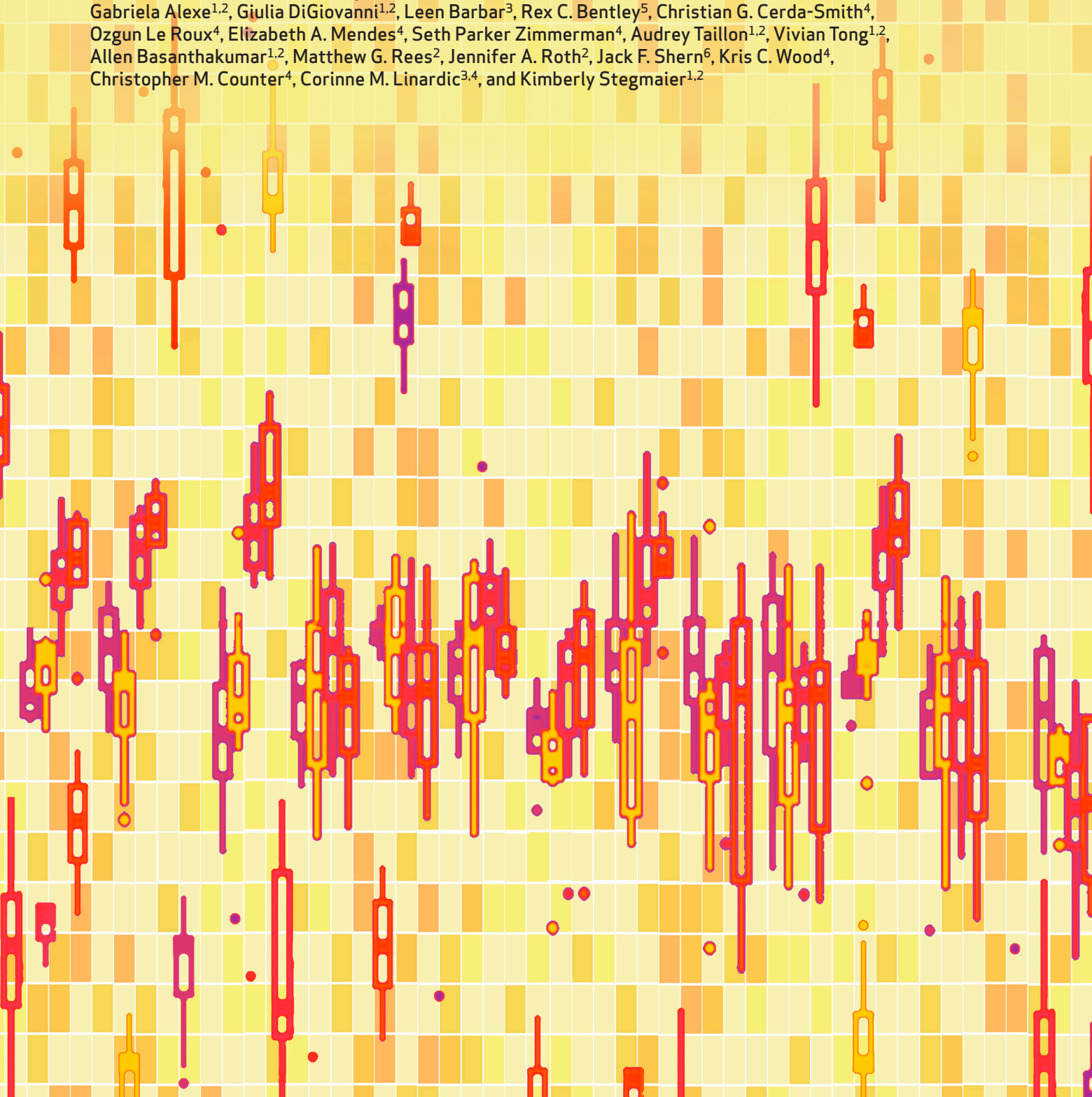
RESEARCH ARTICLE

CDK8 Inhibition Releases the Muscle Differentiation Block in Fusion-Driven Alveolar Rhabdomyosarcoma

Susu Zhang[1,2], Kathleen L. Engel[1,2], Assil Fahs[3], Ara Jo[3], Clare F. Malone[1,2], Kenneth N. Ross[1,2], Marissa Just[3], Brian Guedes[3], Diyana Granum[3], Kristianne M. Oristian[4], Alexander R. Kovach[3], Gabriela Alexe[1,2], Giulia DiGiovanni[1,2], Leen Barbar[3], Rex C. Bentley[5], Christian G. Cerda-Smith[4], Ozgun Le Roux[4], Elizabeth A. Mendes[4], Seth Parker Zimmerman[4], Audrey Taillon[1,2], Vivian Tong[1,2], Allen Basanthakumar[1,2], Matthew G. Rees[2], Jennifer A. Roth[2], Jack F. Shern[6], Kris C. Wood[4], Christopher M. Counter[4], Corinne M. Linardic[3,4], and Kimberly Stegmaier[1,2]



ABSTRACT Alveolar rhabdomyosarcoma (aRMS) is a fusion-driven pediatric cancer with poor survival and limited therapeutic options. To uncover novel vulnerabilities, we used complex-Map functional genomic data, identifying CDK8 as a dependency in aRMS. Both *CDK8* knockout and pharmacologic inhibition impaired tumor cell growth and induced myogenic differentiation *in vitro* and *in vivo*. Compared with genetic loss, CDK8 pharmacologic inhibition induced more dynamic transcriptional changes. With a genome-scale CRISPR–Cas9 drug modifier screen, we determined that the maximal antitumor activity of the CDK8 inhibitor requires the presence of the Mediator kinase module, including CDK8, and transcriptional cooperation with the SAGA complex. We further identified SIX4 as a key transcription factor mediating CDK8 inhibitor–induced transcriptional activation of myogenic differentiation genes and impaired tumor proliferation. These findings suggest a distinct gain-of-function mechanism of the CDK8 inhibitor and establish a strong rationale for CDK8 inhibition as a differentiation-inducing therapeutic strategy in aRMS.

SIGNIFICANCE: We provide a framework for uncovering therapeutic targets by network-based analysis of functional genomic screens. We identify CDK8 as a druggable target in aRMS and determine that CDK8 inhibition drives myogenic differentiation and impairs tumor progression via a collaborative mechanism involving the Mediator kinase module, SAGA complex, and SIX4.

See related commentary by Stevens and Hatley, p. 2210

INTRODUCTION

Transcription factors are frequently dysregulated in human cancer, leading to abnormal transcriptional programs (1–3). Chromosomal translocations may result in the formation of transcription factor fusion oncoproteins that retain functional domains from two distinct proteins. Fusion oncoproteins are particularly common in pediatric cancers, such as PAX3::FOXO1 in alveolar rhabdomyosarcoma (aRMS; ref. 4). In contrast to kinase-driven cancers, in which small-molecule inhibitors have shown success, pediatric cancers driven by fusion transcription factors present unique therapeutic challenges due to the lack of easily targetable structural pockets and presence of intrinsically disordered domains (5). Additionally, whereas adult cancers often harbor a broad spectrum of mutations that can be therapeutically exploited, pediatric fusion-driven cancers tend to exhibit a low mutational burden, meaning fewer potential targets for precision medicine approaches (6, 7).

Compared with embryonal rhabdomyosarcoma (eRMS), the other major subtype of RMS that lacks a signature driver fusion oncoprotein, aRMS has a worse overall survival. Indeed, aRMS is one of the most difficult to treat childhood cancers. More than 80% of aRMS cases harbor a PAX3/7::FOXO1 fusion, which acts as a novel transcription factor, with altered transcriptional properties compared with either partner transcription factor alone. More than 10,000 potential PAX3::FOXO1 regulatory sites were identified in a recent publication. However, only about 200 gene targets were directly transcriptionally activated by PAX3::FOXO1 based on nascent RNA sequencing (RNA-seq), and most of these direct target genes are also transcription factors (8). Because of the quiet mutational landscape of aRMS and the challenges in targeting transcription factors, either the fusion itself or its downstream targets, current therapy for patients with aRMS is still based on conventional strategies, including chemotherapy, surgery, and radiotherapy, all of which are toxic. Efforts to improve therapeutic response in high-risk patients have included multi-agent, interval-compressed therapy, high-dose chemotherapy with stem cell rescue, oral maintenance regimens, and novel targeted therapies (9). The overall 5-year survival, however, remains poor, and approximately one third of these children will relapse.

Advances in understanding dependencies in pediatric cancers have uncovered critical vulnerabilities within transcriptional machinery, offering promising therapeutic inroads. BET proteins, such as BRD4, have been recognized for their role in

[1]Division of Hematology/Oncology, Department of Pediatric Oncology, Dana-Farber Cancer Institute, Boston Children's Hospital, Harvard Medical School, Boston, Massachusetts. [2]The Broad Institute of MIT and Harvard, Cambridge, Massachusetts. [3]Division of Pediatric Hematology/Oncology, Department of Pediatrics, Duke University School of Medicine, Durham, North Carolina. [4]Department of Pharmacology and Cancer Biology, Duke University School of Medicine, Durham, North Carolina. [5]Department of Pathology, Duke University School of Medicine, Durham, North Carolina. [6]Pediatric Oncology Branch, National Institutes of Health, Bethesda, Maryland.

Current address for K.L. Engel: Cancer Biology, The University of Chicago, Chicago, Illinois.

C.M. Linardic and K. Stegmaier co-senior authors.

Corresponding Authors: Corinne M. Linardic, Linardic Laboratory, Levine Science Research Center, Room B361, 450 Research Drive, Durham, NC 27710. E-mail: corinne.linardic@duke.edu; and Kimberly Stegmaier, Stegmaier Laboratory, Department of Pediatric Oncology, Dana-Farber Cancer Institute, Room LC6113, 360 Longwood Ave, Boston, MA 02215. E-mail: Kimberly_Stegmaier@dfci.harvard.edu

Cancer Discov 2026;16:2344–65

doi: 10.1158/2159-8290.CD-25-1171

This open access article is distributed under the Creative Commons Attribution-NonCommercial-NoDerivatives 4.0 International (CC BY-NC-ND 4.0) license.

©2026 The Authors; Published by the American Association for Cancer Research

regulating transcriptional elongation and enhancer function through regulation of super-enhancers (10, 11). BET inhibitors, however, were met with the challenge of on-target toxicity, including thrombocytopenia, and thus a narrow therapeutic window (12, 13). In contrast, menin inhibitors have emerged as a particularly notable therapeutic success. Menin serves as a key component of the MLL/COMPASS complex and plays an essential role in sustaining KMT2A-fusion transcriptional programs in acute leukemia as well as HOX/MEIS programs in *NPM1*-mutant acute myeloid leukemia (AML; refs. 14, 15). Potent menin inhibitors have demonstrated significant clinical efficacy, earning FDA-approval for *KMT2A*-fusion and *NPM1*-mutant leukemias, marking a breakthrough in the therapeutic targeting of transcriptional coregulators. Notably, these molecules promote myeloid differentiation in AML cells, a feature thought to be critical to their efficacy.

Comprehensive datasets, such as Broad Institute's Dependency Map (DepMap), have emerged as powerful tools for identifying promising single-candidate therapeutic targets in cancer. Coupling the DepMap with network-based analysis allows the identification of codependencies, essential protein complexes and signaling nodes that are critical for cancer cell survival. This approach enables the prioritization of candidate targets based on their functional complexes and interactions within oncogenic pathways (16). For example, the Spt-Ada-Gcn5-acetyltrasferase (SAGA) complex was reported as a dependency in *MYCN*-amplified neuroblastoma, which is driven by an aberrant oncogenic transcriptional program (17). Several members of the complex are modest dependencies, each which individually might have been overlooked, but analysis of complexes highlighted this important neuroblastoma epigenetic regulator. This work also highlighted a framework for uncovering novel druggable targets, particularly in pediatric cancers with low mutational burdens and driven by dysregulated transcriptional machinery.

In the current study, we used an analytic approach to identify dependencies on complexes and nominated the Mediator complex as a dependency in aRMS. We demonstrate that CDK8, a key component of the Mediator kinase module, represents a clinically actionable target in fusion-positive aRMS. Notably, inhibition of CDK8, using a small-molecule inhibitor currently in clinical trials for other diseases, induced *in vivo* differentiation of aRMS tumor cells. Our findings indicate that CDK8 primarily acts as a transcriptional repressor in aRMS, directly repressing the expression of a subset of genes involved in muscle differentiation. Upregulation of the transcription factor SIX homeobox 4 (SIX4), involved in muscle differentiation, is essential to the activity of these CDK8 inhibitors. Most CDK8 inhibitors are ATP-competitive compounds that bind directly to the ATP-binding pocket to halt kinase activity (18, 19). Our findings reveal that CDK8 inhibitors elicit a more potent phenotype than CDK8 genetic deletion and that their efficacy depends on the presence of an intact CDK8 kinase module. These observations support a paradigm of kinase inhibitor trapping, in which the physical presence of the intact but enzymatically inhibited kinase target, and not just inhibition of its catalytic activity alone, is essential for the compound's full potency. Furthermore, the efficacy of CDK8 inhibition is also dependent on the acetyltransferase activity of the SAGA complex, highlighting a cooperative interaction between these transcriptional regulators in the context of the CDK8 inhibitors.

RESULTS

Mediator Complex Catalytic Component CDK8 Is a Selective Dependency in aRMS

To identify novel pharmacologic targets in aRMS, we analyzed the Broad Institute's Cancer DepMap dataset, which includes genome-wide CRISPR–Cas9 screens performed in more than 1,000 human cancer cell line models (https://doi.org/10.25452/figshare.plus.25880521.v1). Utilizing single-sample gene set enrichment analysis (ssGSEA), we systematically assessed protein complex and pathway dependencies in aRMS. We computed the ssGSEA scores to compare aRMS with all other cancer types in DepMap and found that, in aRMS, complexes containing members of the Mediator complex [activator-recruited cofactor (ARC), ARC-L, and ARC92–Mediator] are top hits in ssGSEA based on CORUM-defined complexes (Fig. 1A). We then compared the DepMap dependency scores for the ARC-L–Mediator complex across all tested cancer cell lines, and aRMS also ranked as the disease most dependent on this complex (Supplementary Fig. S1A). Based on the enriched genes in the ssGSEA ARC-L/ARC92–Mediator complex data set (Supplementary Table S1A), we then focused on components of the Mediator kinase module (20–22). The analysis of DepMap also nominated aRMS as the disease most dependent on CDK8, the catalytic subunit of the Mediator kinase module, compared with more than 1,000 tested cell lines across different types of cancers. In contrast, eRMS, the vast majority of which does not express a fusion oncoprotein, ranks like other non–CDK8-dependent malignancies (Fig. 1B). In addition, when focusing on druggable dependencies, we analyzed the DepMap dependency scores of all kinases and compared fusion-positive aRMS with all other tested models and found that CDK8 also scored among the top kinase hits (Fig. 1C). Importantly, we found that other components of the Mediator kinase module, CCNC and MED13, serving as an essential scaffold to stabilize the kinase module within the Mediator complex, also scored as strong selective dependencies in aRMS, underscoring the critical role of the module in this disease (Fig. 1D). Our analysis also showed that non-seminomatous germ cell tumor (TT) cell lines exhibit sensitivity to *CDK8* knockout (KO; Fig. 1B), but we did not observe dependency on the other Mediator kinase module components in non-seminomatous germ cell tumor cell lines.

Building on these findings, we next evaluated the RNA level of *CDK8* in different cancer cell lines using the CCLE 23Q4 dataset and in pediatric tumors using the Treehouse v11 dataset (https://treehousegenomics.soe.ucsc.edu/public-data/). The average *CDK8* transcript levels in RMS are notably elevated compared with other cancer types (Supplementary Fig. S1B and S1C). Protein-level validation using patient-derived xenograft (PDX) tumor microarray samples demonstrated robust expression of CDK8 in aRMS PDX tumors (Supplementary Fig. S1D). In addition, PAX3::FOXO1-expressing aRMS cell lines exhibited higher CDK8 protein levels compared with nontransformed primary human skeletal muscle cells (Supplementary Fig. S1E).

CDK8 Genetic Inhibition Slows aRMS Cell Growth *In Vitro* and *In Vivo*

To evaluate the functional consequences of CDK8 loss of function in aRMS, we used both genetic and pharmacologic approaches. Two independent short hairpin RNAs (shRNA) targeting *CDK8* were used to perturb *CDK8* expression genetically. CDK8 was downregulated effectively at the protein level in Rh28 and Rh30, two fusion-positive aRMS cell lines (Supplementary Fig. S1F). Genetic knockdown of *CDK8* resulted in a marked depression of cell viability (Fig. 1E). More importantly, using an shRNA conditional knockdown system in the Rh28 cell line, we confirmed that *CDK8* depletion significantly inhibited tumor cell growth *in vivo* (Fig. 1F; Supplementary Fig. S1G–S1I). Similarly, CRISPR-mediated genetic KO of *CDK8* led to substantial growth inhibition compared with the cells transduced with control guide RNAs (gRNA) in aRMS cell lines, Rh30 and Rh28 (Fig. 1G; Supplementary Fig. S1J). Furthermore, we examined *CDK8* KO in three additional PAX3::FOXO1-containing aRMS lines (Rh4, RHJT, and JR), one aRMS line with the PAX7::FOXO1 fusion (CW9019), and two fusion-negative eRMS lines (RD and SMSCTR; Supplementary Fig. S1K). We confirmed that *CDK8* KO induced significant growth defects in Rh4 and JR and a more modest response in RHJT (Supplementary Fig. S1L and S1M). The PAX7::FOXO1-containing aRMS cell line CW9019 was not sensitive to *CDK8* KO (Supplementary Fig. S1L and S1M). As predicted by DepMap data, eRMS models, such as RD and SMSCTR, were not responsive to *CDK8* KO (Supplementary Fig. S1N and S1O). To determine whether the proliferation defect is directly due to loss of *CDK8*, we expressed a wild-type (WT) or kinase-dead (D173A) *CDK8* resistant to KO with the CRISPR guide and then evaluated the effect of *CDK8* KO (Supplementary Fig. S1P; refs. 23, 24). The WT *CDK8* fully rescued the growth inhibition caused by *CDK8* CRISPR KO (Fig. 1H). However, we observed a dominant-negative effect of the kinase-dead mutant *CDK8*_KD (D173A), which has been previously reported (23). The expression of the kinase-dead *CDK8* impaired cell growth and failed to rescue the *CDK8* CRISPR KO (Fig. 1H).

CDK8 Pharmacologic Inhibition Slows aRMS Cell Growth *In Vitro* and *In Vivo*

To evaluate the relationship between genetic dependency on *CDK8* and pharmacologic inhibition, we compared DepMap gene-effect scores for *CDK8* KO with Profiling Relative Inhibition Simultaneously in Mixtures (PRISM) data for the CDK8 inhibitor BI-1347. In aRMS, we observed a strong positive correlation (R = 0.68) between these two metrics, whereas the correlation was lower in eRMS (R = 0.32) and other cancer cell lines (R = 0.21; Fig. 2A). Therefore, in addition to genetic manipulation of CDK8 expression, we next tested three selective CDK8 kinase–inhibitory small molecules, including BI-1347, SEL-120-34A, and JH-XII-178, all of which demonstrated on-target activity by reducing $STAT1^{S727}$ phosphorylation (Fig. 2B; ref. 25). In the tested aRMS cell lines, all three CDK8 inhibitors impaired cell growth, whereas the inactive analog of BI-1347, known as BI-1374, exhibited no effect (Fig. 2C and D). Following our observation of the cell growth defect, we assessed for apoptosis by examining Caspase-Glo expression, cleaved PARP levels, Annexin V staining, and cell-cycle phase. Although we observed a mild increase in apoptosis and G2/M phase cell-cycle arrest after genetic or pharmacologic inhibition of CDK8, these effects were insufficient to fully explain the observed growth inhibition (Supplementary Fig. S2A–S2D). To further characterize the impact of CDK8 inhibition, we utilized Incucyte live-cell imaging to monitor cell proliferation. Compared with DMSO, long-term exposure to the CDK8 inhibitors BI-1347, SEL-120-34A, and JH-178 slowed aRMS cell proliferation, suggesting that the primary mechanism of CDK8 inhibition on growth suppression involves reduced proliferative capacity rather than apoptosis or cell-cycle arrest (Fig. 2E; Supplementary Fig. S2E). Lastly, we asked whether CDK8 kinase inhibition conferred antitumor activity in aRMS *in vivo*. We tested the CDK8 inhibitor SEL-120-34A, which has been granted orphan drug designation by the FDA for the treatment of AML and high-risk myelodysplastic syndrome (MDS; https://clinicaltrials.gov), in an Rh30 xenograft model. SEL-120-34A treatment decreased tumor growth *in vivo* without affecting animal weight (Fig. 2F; Supplementary Fig. S2F). Tumors from SEL-120-34A–treated mice exhibited increased cleaved caspase 3 (CC3) staining (Supplementary Fig. S2G and S2H). These data suggest that CDK8 inhibition impairs tumor progression *in vivo* as well as *in vitro*.

CDK8 Inhibition Induces Transcriptional Activation of Myogenic Differentiation–Associated Gene Targets

As CDK8 serves as the catalytic component of the Mediator kinase module, we next performed Precision nuclear Run-On transcription sequencing (PRO-seq) to determine the direct effect of CDK8 inhibition on early events in transcription, particularly RNA polymerase II (Pol II) pausing and elongation (26–28). We analyzed RNA Pol II occupancy using normalized changes in the gene body and by performing differential analysis. We did not observe a global change in RNA Pol II at gene bodies between 4 to 72 hours following BI-1347 treatment in Rh30 cells, indicating that CDK8 kinase inhibition does not lead to a widespread alteration in Pol II transcriptional activity (Fig. 3A; Supplementary Fig. S3A and S3B). There were very few changes noted at the 4-hour time point (Supplementary Fig. S3A). After 24 hours of CDK8 inhibition by BI-1347, however, there were 523 transcripts exhibiting upregulated gene body transcription and 59 transcripts exhibiting downregulated gene body transcription (Fig. 3A and B; Supplementary Table S1B). A similar transcriptional trend was observed at the 72-hour time point after BI-1347 treatment, with 575 transcripts exhibiting upregulated gene body transcription and 193 transcripts exhibiting downregulated gene body transcription (Fig. 3B; Supplementary Fig. S3B; Supplementary Table S1C). These changes at the two treatment time points (24 and 72 hours) were relatively consistent; the dominant effect of CDK8 inhibition was activation of transcription (Supplementary Fig. S3C). When comparing differentially expressed genes identified by PRO-seq with CDK8-bound genes, we found that 65% of upregulated and 44% of downregulated genes were directly associated with CDK8 binding, suggesting a strong correlation between CDK8 occupancy and its transcriptional regulatory effects (Supplementary Fig. S3D). The heatmaps of the normalized RNA Pol II

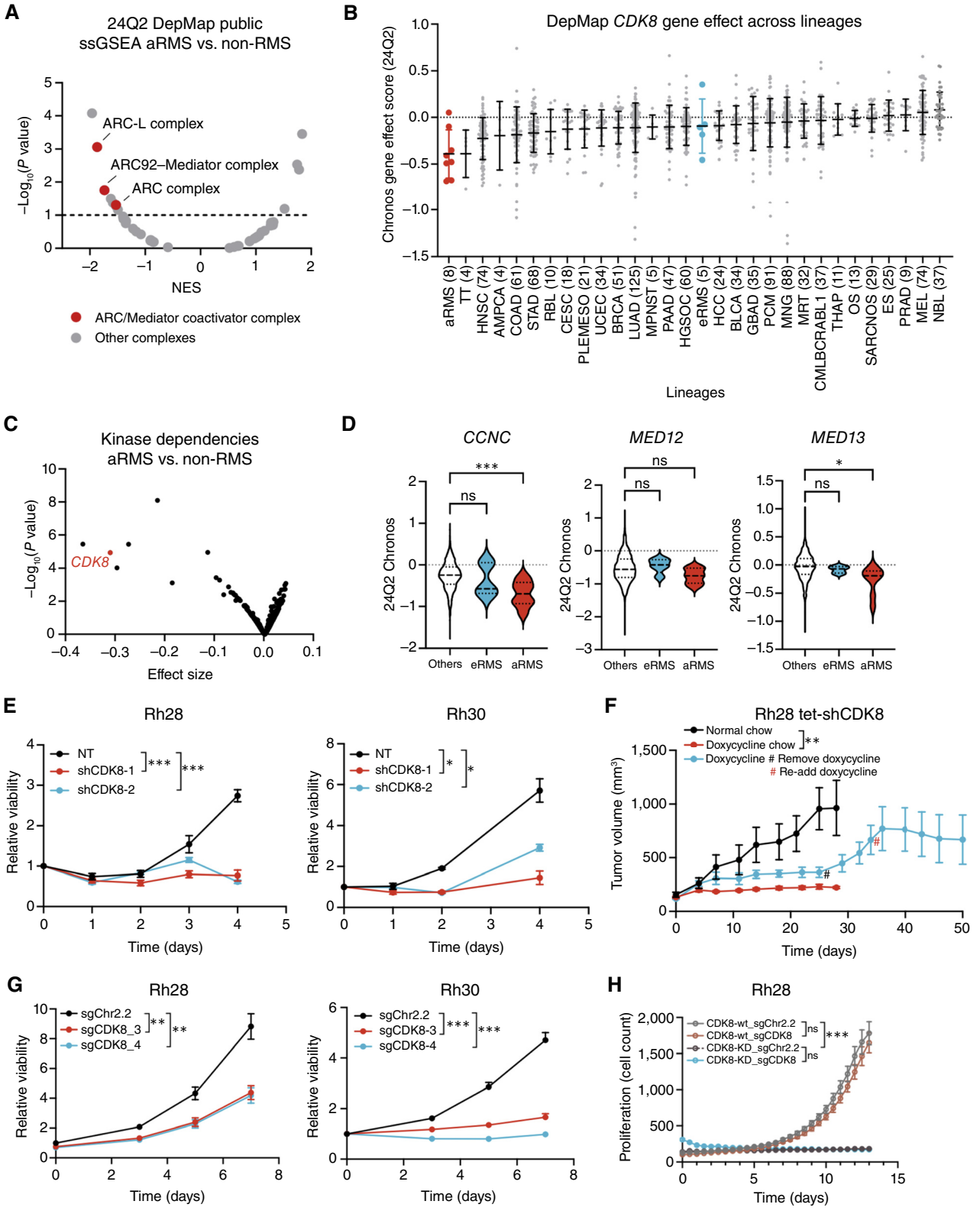


Figure 1. Mediator complex catalytic component CDK8 is a selective dependency in aRMS. **A,** ssGSEA on genome-wide differential effect size of CORUM complexes comparing aRMS with other non-RMS tumor cell lines. Red indicates the Mediator complex. Significance for ssGSEA method: NES < −1.5, *P* value < 0.10. **B,** Distribution of *CDK8* gene effect scores across different cancer cell lines from the Broad Institute's CRISPR DepMap (24Q2). Data are presented as the mean ± SD. **C,** Dot plot of kinase dependencies in the Broad Institute's CRISPR DepMap comparing fusion-positive aRMS with all other cancer cell lines. *CDK8* is highlighted in red. Significance: effect size < −0.25, *P* value < 0.10. (*continued on following page*)

occupancy and pausing index indicated increased occupancy of RNA Pol II along the gene body at the changed genes defined by PRO-seq, further suggesting increased transcriptional elongation at gene bodies (Fig. 3C; Supplementary Fig. S3E). The steady-state RNA levels, as assessed by whole-transcriptome RNA-seq, correlated with the changes observed in the nascent transcription analysis, demonstrating concordance between nascent and steady-state RNA levels (Fig. 3D).

Although global RNA Pol II occupancy at gene bodies remained largely unchanged following BI-1347 treatment, transcriptional regulation can also occur at the enhancer level. To further elucidate the transcriptional mechanisms underlying CDK8 inhibition, we utilized the previously obtained PRO-seq data to quantify enhancer RNA (eRNA) expression following CDK8 inhibition. After 24 hours of BI-1347 treatment, there were 1,380 eRNAs with increased expression, whereas only 100 had decreased expression (Fig. 3E). We then evaluated for activated enhancers by assessing for chromatin accessible regions by Assay for Transposase-Accessible Chromatin using sequencing (ATAC-seq). Consistent with the PRO-seq analysis, although we did not observe global changes in chromatin accessibility, we did identify focal gains in chromatin accessibility (2,831 increased peaks vs. 174 decreased peaks), predominantly (>90%) in intergenic or intronic regions (Fig. 3F and G; Supplementary Fig. S3F). To confirm that these regions with increased accessibility were undergoing nascent transcription, we then plotted the PRO-seq signal ± 2.5 kb at these upregulated ATAC-seq peaks, with the histogram showing an increase in active polymerase around these upregulated ATAC-seq regions after 24 and 72 hours of CDK8 inhibition (Fig. 3H). These findings suggest that CDK8 inhibition does not globally affect transcriptional activities at gene bodies or enhancers but instead selectively activates the transcription of specific genes by enhancing eRNA production and activity.

GSEA revealed a strong overlap between transcriptional changes driven by *CDK8* genetic KO (sgCDK8) and BI-1347 treatment (Supplementary Fig. S3G). To further annotate the changes induced by BI-1347, we performed GSEA on genes identified to be up regulated in the 24-hour PRO-seq data. Notably, early transcriptional activation at 24 hours of BI-1347 treatment was enriched for muscle-related pathways, including muscle tissue development and muscle cell differentiation, as well as other annotations related to muscle cell development with C5 ontology gene sets (Fig. 3I). Similarly, RNA-seq data generated following *CDK8* KO highlighted genes associated with myogenesis as the top upregulated signature (Supplementary Fig. S3H). In further support of a differentiation phenotype, BI-1347 treatment increased expression of the skeletal muscle–related myosin heavy chain (MYH) genes, including *MYH1-4*, *MYH8*, and *MYH13* but not cardiac muscle–related *MYH6* or other nonmuscle MYH genes (Fig. 3J; refs. 29, 30). Consistent with these PRO-seq and RNA-seq results, the muscle differentiation marker MYH (MF20) as assessed by immunofluorescence was elevated after treatment with BI-1347 and SEL-120-34A (Fig. 3K; Supplementary Fig. S3I). Inverted microscopy imaging and phalloidin staining revealed that both BI-1347 treatment and *CDK8* KO induced morphologic changes consistent with cell differentiation (Fig. 3K; Supplementary Fig. S3J). Moreover, the transcription factor MEF2C, which is critical for skeletal muscle differentiation, was also upregulated upon CDK8 inhibition (Supplementary Fig. S3K). Importantly, upon *CDK8* genetic inhibition, we observed increased cytoplasmic eosin staining with eccentrically located nuclei structures in the xenograft tumor samples, indicative of myofibril generation, a morphologic hallmark of myogenic differentiation *in vivo* (Fig. 3L; Supplementary Fig. S3L; ref. 31). In addition, tumors from these mice exhibited increased myoglobin mRNA expression when CDK8 was repressed (Fig. 3M). These findings demonstrate that both *in vitro* and *in vivo* CDK8 inhibition induces evidence of muscle differentiation.

CDK8 Inhibition Does Not Function Directly through PAX3::FOXO1-Regulated Core Enhancers in aRMS

To assess whether CDK8 inhibition affects the expression of or the binding to the targets of PAX3::FOXO1, the most common fusion oncoprotein driving aRMS, we first examined whether CDK8 inhibition impacts mRNA levels of the fusion gene. We did not observe changes in *PAX3::FOXO1* gene body transcription following BI-1347 treatment for up to 72 hours (Fig. 4A). In addition to its role in Mediator function, CDK8 has also been reported to phosphorylate transcription factors (25). A kinase prediction tool indicated that a phosphorylation site on WT FOXO1 is a predicted site of CDK8, and this site is preserved in the PAX3::FOXO1 protein (FOXO1^{Ser479}; https://gps.biocuckoo.cn/index.php). Although there is currently no available antibody to interrogate this Ser479 phosphorylation site, given that the phosphorylation event might affect PAX3::FOXO1 stabilization and/or cytoplasmic–nuclear transport, we examined levels of PAX3::FOXO1 protein after

Figure 1. ***(Continued)*** **D,** Violin plots showing distribution of *CCNC*, *MED13*, and *MED12* gene effect scores from the DepMap (24Q2) comparing the fusion-positive aRMS and fusion-negative eRMS with all other indicated cancer cell lines. aRMS is highlighted in red, and eRMS is highlighted in blue. (*, $P \leq 5.0e{-}02$; ***, $P \leq 1.0e{-}03$). **E,** shRNA-mediated suppression of *CDK8* by two different shRNAs impairs Rh30 and Rh28 aRMS cell growth *in vitro*. Cell numbers were determined by Trypan Blue live-cell counting. Data are presented as the mean ± SEM ($n = 3$; AUC *, $P \leq 5.0e{-}02$; **; $P \leq 1.0e{-}02$; ***, $P \leq 1.0e{-}03$). **F,** Line graph showing mean subcutaneous tumor volume (mm^3) formed by Rh28 cells after treatment with inducible knockdown of CDK8 using shRNA. Data are presented as the mean ± SEM (n_normal = 7, n_doxycycline = 7, n_variable = 3; AUC **, $P \leq 1.0e{-}02$). **G,** CRISPR-mediated KO of *CDK8* by two different gRNAs impairs Rh30 and Rh28 aRMS cell growth *in vitro*. Relative growth was assessed by CellTiter-Glo after CRISPR KO. Data are presented as the mean ± SEM (n_Rh28 = 6, n_Rh30 = 16; AUC **, $P \leq 1.0e{-}02$; ***, $P \leq 1.0e{-}03$). **H,** Live-cell proliferation assessed by Incucyte for Rh28 cells with overexpression of *CDK8* WT or kinase-dead + sgChr2.2 or sgCDK8-3. Data are presented as the mean ± SEM ($n = 3$; AUC ***, $P \leq 1.0e{-}03$). AMPCA, ampullary carcinoma; BLCA, bladder urothelial carcinoma; BRCA, breast carcinoma; CESC, cervical squamous cell carcinoma; CMLBCRABL1, chronic myeloid leukemia, BCR-ABL1+; COAD, colon adenocarcinoma; ES, Ewing sarcoma; GBAD, gallbladder adenocarcinoma; HGSOC, high-grade serous ovarian cancer; HNSC, head and neck squamous cell carcinoma; HCC, hepatocellular carcinoma; LUAD, lung adenocarcinoma; MEL, melanoma; MPNST, malignant peripheral nerve sheath tumor; MNG, meningioma; MRT, malignant rhabdoid tumor; NBL, neuroblastoma; ns, not significant; OS, osteosarcoma; PAAD, pancreatic adenocarcinoma; PCM, plasma cell myeloma; PLEMESO, pleural mesothelioma; PRAD, prostate adenocarcinoma; RBL, retinoblastoma; SARCNOS, sarcoma, not otherwise specified; STAD, stomach adenocarcinoma; THAP, anaplastic thyroid cancer; TT, testicular teratoma; UCEC, endometrial carcinoma.

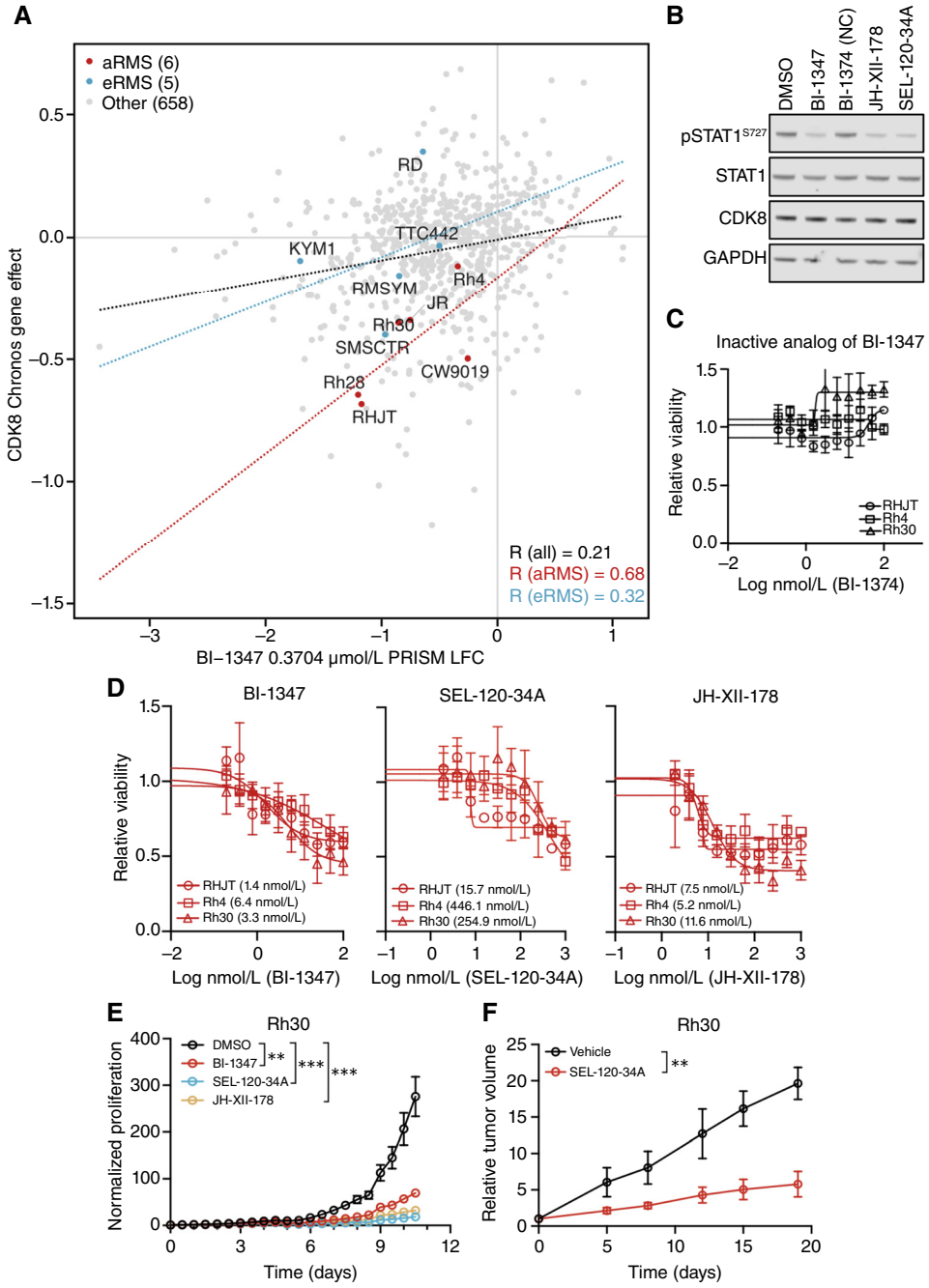


Figure 2. Pharmacologic inhibition of CDK8 in fusion-positive aRMS impairs cell growth *in vitro* and *in vivo*. **A,** Correlation between *CDK8* gene dependency and sensitivity to the CDK8 inhibitor BI-1347 in 669 cancer cell lines (*y*-axis showing CDK8 dependency score; *x*-axis showing PRISM LFC value of BI-1347 treatment). Linear regression lines and Pearson correlation coefficients (R) are shown for all cell lines (black), aRMS (red), and eRMS (blue). **B,** Western blot analysis showing CDK8 inhibition by small molecules as assessed by STAT1 phosphorylation at serine 727. **C** and **D,** Dose–response curves of inactive BI-1347 analog (BI-1374; **C**) and three pharmacologic CDK8 inhibitors (**D**), BI-1347, SEL-120-34A, and JH-XII-178, at day 7 of treatment in Rh30, Rh4, and RHJT cell lines; IC_{50} values are shown in parentheses ($n = 4$). **E,** Live-cell proliferation assessed by Incucyte for Rh30 cells after treatment with vehicle DMSO (black), the CDK8 inhibitor BI-1347 (red), SEL-120-34A (blue), and JH-178 (yellow). Data were normalized to DMSO. Data represent the means ± SEM ($n = 3$; AUC **, $P \leq 1.0e{-}02$; ***, $P \leq 1.0e{-}03$). **F,** Line graph reveals mean subcutaneous relative tumor volume to the starting volume for Rh30 cells after treatment with the CDK8 inhibitor SEL-120-34A. Data are presented as the mean ± SEM (n_vehicle = 5, n_SEL-120-34A = 9; endpoint **, $P \leq 1.0e{-}02$).

treatment with the CDK8 inhibitor BI-1347. Neither total PAX3::FOXO1 protein levels nor its nuclear or cytoplasmic distribution was altered by CDK8 inhibition (Supplementary Fig. S4A).

Previous studies reported CDK8 among the proteins in proximity to endogenous PAX3::FOXO1, and CDK8 was enriched in binding at high-confidence PAX3::FOXO1-regulated enhancers (8). To verify this interaction, we first

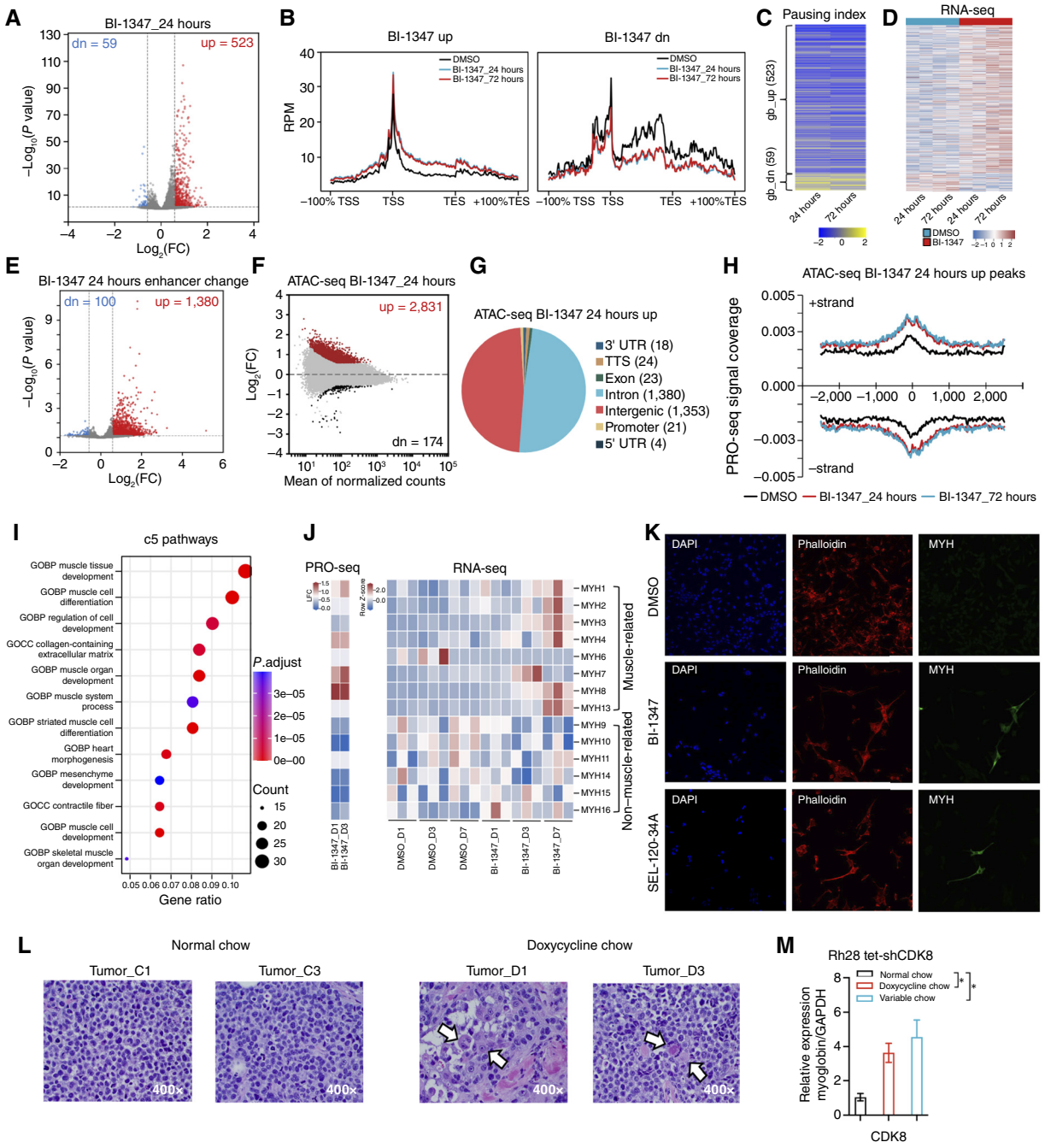


Figure 3. CDK8 inhibition induces transcriptional activation of myogenic differentiation–associated genes. **A,** Volcano plots showing the number of gene body changes after 24 hours of CDK8 inhibitor BI-1347 treatment. Significantly upregulated genes are highlighted in red; significantly downregulated genes are highlighted in blue (P adj < 0.05, FC >1.5 or < −1.5). **B,** Metagene plots of PRO-seq reads of genes with significant upregulation or downregulation of gene body transcription at 24 hours of BI-1347 treatment. **C,** Heatmap of $\log_2$-transformed FC values of PRO-seq pausing indices of genes with changes in gene body transcription at the 24-hour time point. **D,** Heatmap showing $\log_2$-transformed FC of RNA-seq read counts for indicated gene sets after DMSO and BI-1347 (10 nmol/L) treatment for 24 or 72 hours. **E,** Volcano plots reveal the number of changes in eRNA transcripts after 24 hours of BI-1347 treatment. Significantly upregulated eRNAs are highlighted in red; significantly downregulated eRNAs are highlighted in blue (P adj < 0.05, FC >1.5 or < −1.5). **F,** MA plots showing the changes of chromatin accessibility by ATAC-seq following 4 and 24 hours of BI-1347 treatment. Significantly increased ATAC-seq peaks are highlighted in red; significantly decreased ATAC-seq peaks are highlighted in black (P adj < 0.05, FC >1.5 or < −1.5). **G,** Pie chart showing the peak annotation of upregulated ATAC-seq peaks to gene features at 24 hours of BI-1347 treatment. **H,** Histogram of PRO-seq reads around upregulated ATAC-seq peaks at indicated time points of BI-1347 treatment. **I,** Bubble plot showing PRO-seq gene sets enriched by GSEA that are upregulated at 24 hours. Dot size indicates number of genes in each gene set, and dot color indicates P adjusted value. **J,** Heatmaps of PRO-seq $\log_2$-transformed FC and row z-score–normalized RNA-seq counts of MYH genes. **K,** Immunofluorescence analysis of MYH (MF20; green; 20×) in Rh30 cells after 21 days of DMSO, BI-1347, or SEL-120-34A treatment. **L,** Representative images of hematoxylin and eosin stain of Rh28 xenograft tumors. Doxycycline chow induces expression of the CDK8-directed shRNA. Arrows indicate myofibrils. **M,** Relative expression of myoglobin mRNA level assessed by qPCR in Rh28 xenograft tumor samples. Data are presented as the mean ± SEM ($n = 3$; *, $P \leq 5.0e{-}02$). dn, downregulated; up, upregulated; UTR, untranslated region.

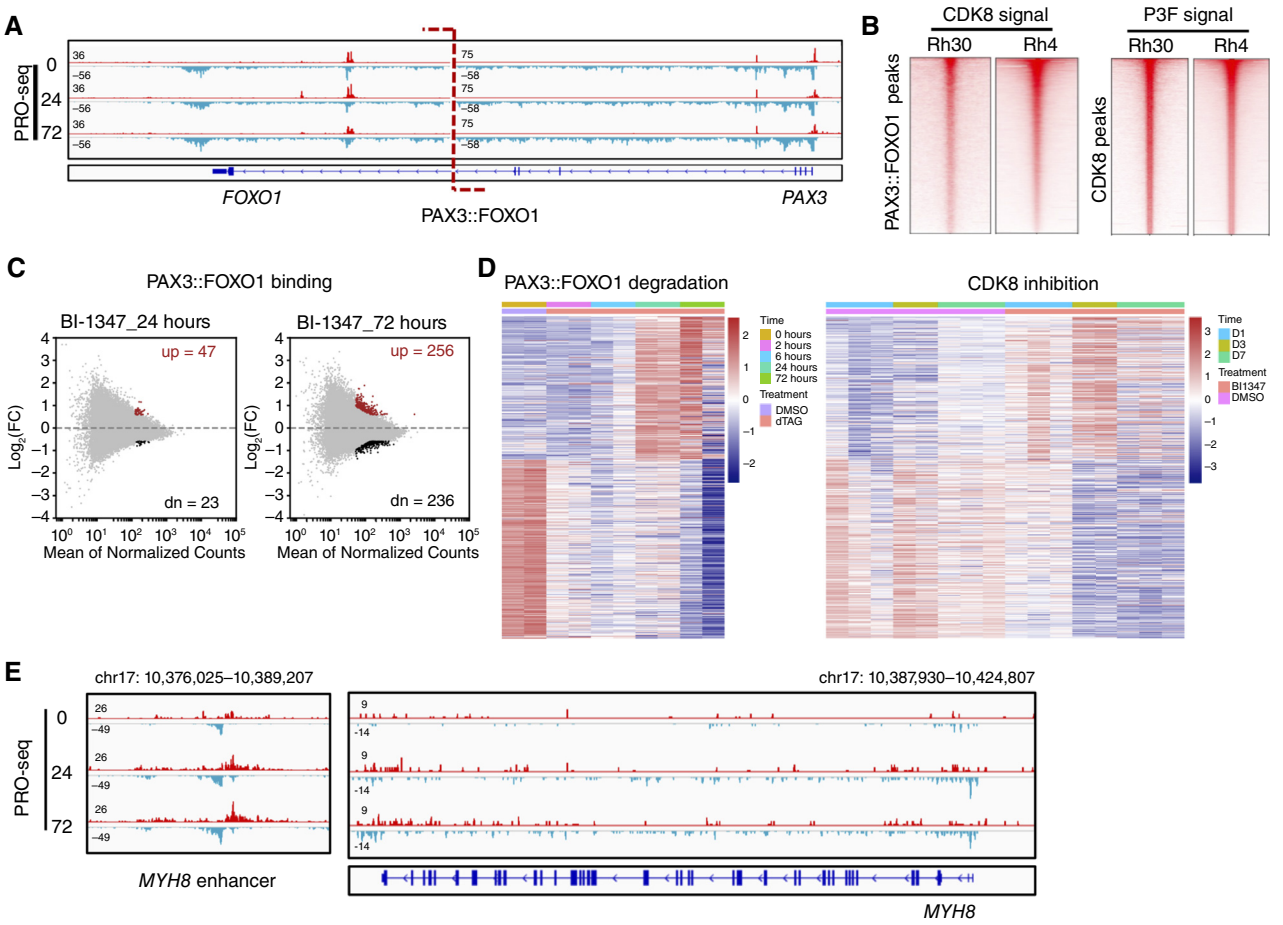


Figure 4. CDK8 inhibition induces a differentiation program without altering PAX3::FOXO1. **A,** IGV gene tracks showing a time course analysis of BI-1347 treatment by PRO-seq signal at the *PAX3::FOXO1* locus. **B,** Heatmaps of CUT&RUN analysis of CDK8 and PAX3::FOXO1 binding in Rh30 and Rh4 cell lines. **C,** MA plots showing changes of PAX3::FOXO1 binding following BI-1347 treatment at 24 and 72 hours. Significantly increased PAX3::FOXO1 peaks are highlighted in red; significantly decreased PAX3::FOXO1 peaks are highlighted in black (P adj < 0.05, FC >1.5 or < −1.5). **D,** Heatmaps of $\log_2$-transformed FC of RNA-seq read counts plotted by the shared gene between 24 hours of PAX3::FOXO1 degradation and 72 hours of CDK8 inhibition at the indicated time points. **E,** IGV gene tracks showing a time course analysis for PRO-seq signal at the *MYH8* locus after BI-1347 treatment. dn, downregulated; up, upregulated.

performed BioID protein-proximity labeling in HEK293T cells expressing Myc-BirA_PAX3::FOXO1 or a Myc-BirA control and in mock control cells (Supplementary Fig. S4B). Stable expression of the Myc-BirA_PAX3::FOXO1 fusion, Myc-BirA, and biotinylation were further confirmed by confocal immunofluorescent imaging (Supplementary Fig. S4C). Streptavidin affinity pulldown followed by quantitative LC–MS/MS identified CDK8 peptides as one of the top hits other than the PAX3::FOXO1 peptides (Supplementary Fig. S4D; Supplementary Table S1D), consistent with the previously reported PAX3::FOXO1-binding proteins, including CDK8, identified by APEX2 proximal labeling in Rh30 cells (8). Moreover, given that the Mediator complex is involved in facilitating promoter–enhancer interactions, and that CDK8 showed enrichment at PAX3::FOXO1-regulated enhancers, we next evaluated whether PAX3::FOXO1 binding changes globally or at PAX3::FOXO1-regulated enhancers after CDK8 inhibition or KO. Consistent with the previously reported study of PAX3::FOXO1 endogenous degradation, CDK8 colocalized with PAX3::FOXO1 (Fig. 4B; ref. 8). To more accurately detect PAX3::FOXO1 changes on chromatin, we next used an epitope-tagged PAX3::FOXO1_FKBP-HA cell line (8) and HA antibody to map PAX3::FOXO1 genome binding following CDK8 inhibition. We found only minimal changes in PAX3::FOXO1 binding after CDK8 inhibition at 24 and 72 hours (Fig. 4C). For the high-confidence PAX3::FOXO1-regulated enhancers defined previously (115 peaks; ref. 8), neither CDK8 binding [Supplementary Fig. S4E (left)] nor PAX3::FOXO1 [Supplementary Fig. S4E (right)] binding was affected by CDK8 inhibition. These results indicate that the impact of CDK8 inhibition on FP-RMS cell biology may not function directly through PAX3::FOXO1-regulated core enhancers. However, RNA-seq revealed shared transcriptional changes between CDK8 inhibition and PAX3::FOXO1 degradation over long-term treatment, manifested by an enrichment in genes associated with muscle differentiation, such as *MYH8*, *VGLL2*, *MYL1*, and *MYBPH* (Fig. 4D and E; Supplementary Fig. S4F–S4I).

Interruption of the SAGA Complex Is Sufficient to Rescue the Impaired Growth Induced by CDK8 Inhibitors

To gain insight into mechanisms of resistance or sensitization to CDK8 inhibitors in aRMS, we performed a genome-scale CRISPR–Cas9 drug modifier screen against the CDK8 inhibitor BI-1347. We generated an Rh30-Cas9-mCherry cell line and transduced it with the Avana-4 single-guide RNA (sgRNA) library (32). The transduced cells were further divided into two groups, DMSO and BI-1347, and treated for 21 days (Supplementary Fig. S5A). We collected cells on days 14 and 21 to measure sgRNA abundance and identify potential modifiers. We first intersected the top 10 hits detected from days 14 and 21 to confirm the robustness and reproducibility of the screen (Fig. 5A; Supplementary Fig. S5B and S5C; Supplementary Table S1E and S1F). We further analyzed the pathways enriched with resistance to 21 days of BI-1347 treatment using the GSEA C5 gene sets. The most enriched gene signatures were associated with SAGA (Spt-Ada-Gcn5 acetyltransferase) coactivator complex or transcriptional activation (Fig. 5B). Notably, three of the top six shared genes are components of the SAGA coactivator complex: TADA2B and KAT2A forming part of the histone acetyltransferase (HAT) module, and TAF5L belonging to the core module (Fig. 5C). Additionally, SGF29 from the HAT module and SUPT20H from the core module were also among the shared hits identified at both days 14 and 21 (Fig. 5C). Resistance hits (genes whose KO rescued growth under BI-1347 treatment) scored higher than sensitizing hits (genes whose KO enhanced BI-1347 sensitivity) in our screen (Fig. 5A; Supplementary Fig. S5B and S5C).

To validate these findings, we first examined the muscle differentiation–associated genes induced by CDK8 inhibition as defined by PRO-seq, such as *RUNX1*, *SEMA3D*, *VGLL2*, and *MYL1*. Induction of their expression by CDK8 inhibitors was reversed upon disruption of KAT2A/B using a proteolysis-targeting chimera (PROTAC), GSK699 (33), as evidenced at both mRNA and protein levels (Fig. 5D; Supplementary Fig. S5D and S5E). We then conducted cell proliferation assays using Incucyte live-cell imaging to evaluate BI-1347 and SEL-120-34A treatment in the context of KO of members of the SAGA complex in Rh30 cells. As shown previously in Fig. 2E, these CDK8 inhibitors slowed proliferation in Rh30 cells. Then, we used two gRNAs to target *TAF5L* and *TADA2B*, and GSK699 (KAT2A/B PROTAC), to disrupt these members of the SAGA complex. Consistent with the screen results, all three SAGA components when depleted rescued the proliferation defect induced by CDK8 inhibitors (Fig. 5E–G; Supplementary Fig. S5F–S5J). A top rescue hit from the CRISPR screen, TADA2B, was validated in a second aRMS cell line, Rh28 (Fig. 5H). Consistently, Incucyte live-cell imaging further showed that the CDK8 inhibition–associated growth defects and morphologic changes were rescued upon SAGA complex disruption (Supplementary Fig. S5K). To determine whether SAGA complex disruption rescues CDK8 inhibition–induced growth defects *in vivo*, we established an Rh28 xenograft mouse model harboring either *TADA2B* KO (sg*TADA2B*) or a *Chr2.2* control KO (sg*Chr2.2*). Whereas SEL-120-34A treatment reduced tumor volume in sg*Chr2.2* cells, sg*TADA2B* rescued this effect, preventing the tumor growth inhibition observed with CDK8 inhibition (Fig. 5I). Together with the PRO-seq data, these findings support a transcriptional repressive role of CDK8 in aRMS and the requirement of the SAGA complex for induction of differentiation associated genes and the proliferative defect upon CDK8 inhibition in aRMS.

CDK8 Inhibition Induces Increased Binding of SIX4 and the SAGA Complex to Muscle Differentiation Genes

Our findings indicate that CDK8 inhibition predominantly leads to transcriptional activation, with the SAGA transcriptional coactivator complex playing a critical role in mediating this effect. We next asked whether there is a specific transcription factor(s) involved in this regulation. Our screen on both days 14 and 21 identified the transcription factor SIX4, reported to play a critical role in myogenic differentiation, as a top transcription factor gene hit (Supplementary Fig. S5B and S5C; Supplementary Table S1E and S1F; refs. 34, 35). Incucyte analysis showed that KO of *SIX4* partially rescued the growth inhibition caused by CDK8 inhibition (Fig. 6A; Supplementary Fig. S6A and S6B). Total protein levels of SIX4 increased after treatment with each of the three CDK8 inhibitors (Fig. 6B), and SIX4 was predominantly localized to the nucleus (Fig. 6C). Consistently, CDK8 inhibitors also elevated *SIX4* mRNA levels as detected by both PRO-seq [4-hour $\log_2$ fold change (LFC) = 0.293, 24-hour LFC = 0.4, and 72-hour LFC = 0.306] and RNA-seq (24-hour LFC = 0.687, 72-hour LFC = 0.642, and day-7 LFC = 0.488; Supplementary Fig. S6C). We next examined the localization of SIX4 and the SAGA component TADA2B on chromatin by cleavage under targets and release using nuclease (CUT&RUN) to further characterize their roles in CDK8-mediated transcriptional regulation. Following BI-1347–mediated CDK8 inhibition, we observed an increase in SIX4 and TADA2B binding on chromatin (Fig. 6D and E). Peak annotation using Homer analysis revealed that nearly 90% of the increased binding peaks for both SIX4 and TADA2B were annotated to intronic or intergenic regions (Fig. 6F and G), whereas the overall SIX4 and TADA2B binding sites are evenly distributed among promoter, intronic, and intergenic regions (Supplementary Fig. S6D). Accordingly, we found that the increase in SIX4 and TADA2B binding with CDK8 inhibitor treatment correlated with enhanced chromatin accessibility identified by ATAC-seq, as well as increased H3K27ac (Fig. 6H; Supplementary Fig. S6E and S6F). Given that the SAGA complex is responsible for H3K9 acetylation, we also investigated H3K9ac after 24 hours of BI-1347 treatment. No notable differences were detected either globally or at the specific sites in which SIX4 binding is increased (Supplementary Fig. S6G). Examination of key skeletal muscle development–related genes, such as *MYH8* and *RUNX1*, illustrates the dynamics of these changes (Fig. 6I; Supplementary Fig. S6H). By 24 hours of CDK8 inhibition, eRNA transcription increased at upstream intergenic enhancers of *MYH8* and *RUNX1*. These regions also exhibited upregulated binding of SIX4 and TADA2B, correlating with active transcription of *MYH8* and *RUNX1* gene bodies (Fig. 6I; Supplementary Fig. S6H).

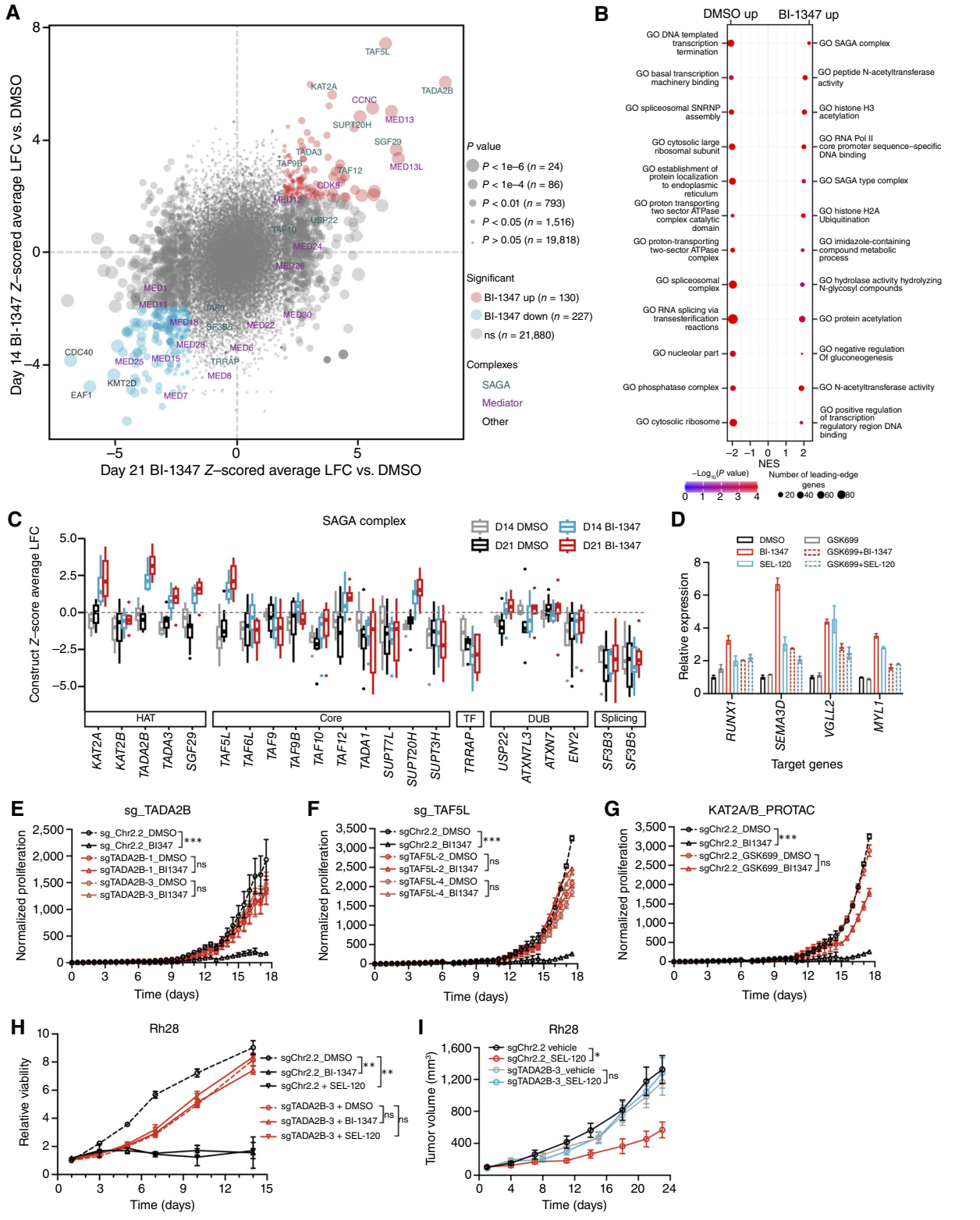


Figure 5. Interruption of the SAGA complex rescues the inhibitory effect of CDK8 inhibitors on the growth of aRMS cells. **A,** Scatter plot showing the Z-scored average LFC of gene KO effects in Rh30 cells treated with BI-1347 vs. DMSO at day 14 (*y*-axis) and day 21 (*x*-axis) from genome-wide CRISPR-Cas9 screens. Each point represents an individual gene; dot size corresponds to statistical significance, and dot color indicates classification. **B,** Bubble plot of C5 gene sets enriched in GSEA at day 21 in the CRISPR-Cas9 BI-1347 drug modifier screen. **C,** Box and whisker plots showing construct-level Z-score averages for individual genes in the SAGA complex from the genome-wide CRISPR-Cas9 screen in Rh30 cells treated with DMSO (gray/black) or BI-1347 (blue/red) for 14 days (gray and blue) or 21 days (black and red). Genes are grouped by SAGA functional modules. (*continued on following page*)

The CDK8 Kinase Module Is Required for Maximal CDK8 Inhibitor Activity

Unexpectedly, MED13 and CCNC, key components of the Mediator CDK8 kinase module, emerged as two of the top six shared rescue gene hits between days 14 and 21 in the genome-scale CRISPR–Cas9 BI-1347 drug modifier screen (Fig. 5A; Supplementary Fig. S5B and S5C). A detailed analysis of the gRNA abundance targeting all kinase module members revealed enrichment after 21 days of BI-1347 treatment, especially for guides directed against *CCNC*, *MED13*, and *MED13L* (Fig. 7A). In contrast to our results for the SAGA complex and *SIX4*, in which KO of these genes does not affect growth in DMSO-treated samples, KO of *CDK8*, *CCNC*, *MED13*, or *MED12* impairs growth in the vehicle-treated condition (Fig. 7A, comparing the gray/black box with the gray dashed line), recapitulating the DepMap findings and our validation studies of the *CDK8* dependency in aRMS (Fig. 1A–G). We validated the dependency on *CCNC* in addition to *CDK8* when comparing the abundance of gRNAs on days 0 and 21 of DMSO treatment (Fig. 7A). In addition, Incucyte assays further substantiated the dependency on *CDK8* and *CCNC* in the Rh30 cell line (Fig. 7B; Supplementary Fig. S7A). When comparing the relative proliferation rate, however, genetic KO of *CDK8* and *CCNC* partially rescued the inhibitory effects of BI-1347 (Fig. 7B). We validated the rescue of BI-1347 with *CCNC* KO in a second cell line, Rh28 (Supplementary Fig. S7B). RNA-seq analysis revealed only minor changes in the RNA levels of *CDK8*, *MED12*, *MED13*, *MED13L*, and *CCNC* after CDK8 inhibition or genetic KO (Supplementary Fig. S7C). In contrast, the protein levels of these genes were increased after prolonged (14 days) CDK8 inhibition with three different CDK8 inhibitors (Supplementary Fig. S7D).

Lastly, we investigated whether the chromatin binding of Mediator kinase module components was altered with CDK8 inhibitor treatment. We performed CUT&RUN with antibodies against CDK8, CCNC, MED12, and MED13 after BI-1347 treatment for 24 hours. In parallel, we profiled MED1 to determine whether other Mediator modules undergo similar chromatin occupancy changes. As expected, there were no significant global changes in chromatin binding of CDK8, CCNC, MED12, MED13, or MED1 (Fig. 7C; Supplementary Fig. S7E–S7G). However, we observed site-specific increases in binding of the Mediator kinase module and MED1 (Fig. 7C; Supplementary Fig. S7E–S7H). Notably, HOMER motif analysis revealed that CDK8-bound regions with increased occupancy upon CDK8 inhibition were enriched for motifs associated with myogenic differentiation such as RUNX1 and MYOG (Fig. 7D). Moreover, at SIX4-upregulated loci, we detected increased chromatin occupancy of CDK8, CCNC, MED12, MED13, and MED1 (Fig. 7E), a pattern that was similarly observed at sites with increased TADA2B binding (Supplementary Fig. S7H). For instance, at the *RUNX1* locus, the upstream enhancer and gene body region showed active transcription, accompanied by increased Mediator kinase components and MED1 at the enhancer (Fig. 7F). In contrast, no changes in Mediator kinase component binding were observed at PAX3::FOXO1-regulated core enhancers, such as a *RUNX2* super-enhancer locus (Supplementary Fig. S7I and S7J). These findings suggest that CDK8 inhibition does not broadly alter chromatin occupancy of the Mediator kinase/Mediator module. Rather, CDK8 small-molecule inhibitors selectively increase Mediator kinase, Mediator, and the SAGA complexes, and SIX4 on chromatin at differentiation-associated enhancers, facilitating transcriptional activation of myogenic genes and contributing to the prodifferentiation effects of CDK8 inhibition in aRMS.

DISCUSSION

Previous studies established that CDK8 functions as a transcriptional repressor by modulating RNA Pol II activity or by phosphorylating transcription factors (20, 25, 36). In yeast, Mediator complexes with and without the CDK8 kinase module were identified, with the majority of Pol II and MED26-containing complexes lacking the CDK8 module (37–39). This modularity highlights CDK8 as a reversible molecular switch that fine-tunes transcription reinitiation by restricting Pol II interactions with the core Mediator complex (20, 40, 41). Furthermore, CDK8 has been shown to inhibit the kinase activity of general transcription initiation factor IIH, thereby modulating transcription initiation (42). This enhancer–Mediator–Pol II interplay is crucial for regulating transcriptional programs, as demonstrated in naïve pluripotent stem cells, in which CDK8 inhibition activates pluripotency-associated transcription (43–45). Similarly, this principle is also demonstrated in AML, in which super-enhancer–associated genes are upregulated upon CDK8 inhibition (44).

Our findings provide compelling evidence that the CDK8 inhibitor BI-1347 releases transcriptional repression in aRMS, in which CDK8 is more highly expressed compared with human skeletal muscle cells and other types of tumors, in part by derepressing differentiation-related transcriptional programs. These observations align with previous studies showing that CDK8 represses differentiation pathways to sustain the oncogenic properties of stem- or progenitor-like cells in various cancers (46, 47). Phenotypically, we observed a proliferation defect and promotion of cell differentiation after CDK8 inhibition, findings supported by the upregulation

Figure 5. ***(Continued)*** Boxes indicate the median and interquartile range (IQR; 25th–75th percentile); whiskers extend to 1.5× the IQR. Values beyond the end of the whiskers are plotted individually. **D,** Quantitative real-time TaqMan qPCR analysis of *RUNX1*, *SEMA3D*, *VGLL2*, and *MYL1* expression at day 7 following treatment with vehicle control (DMSO), CDK8 inhibitors, or GSK699 and the indicated combination treatments. Expression levels were normalized to *GAPDH* gene expression and shown relative to DMSO control. Data represent the means ± SEM ($n = 3$; Statistics analysis is showed in Supplementary Table S1G. **E–G,** Live-cell proliferation assessed by Incucyte for BI-1347 ± sgTADA2B (**E**), BI-1347 ± sgTAF5L (**F**), and BI-1347 ± GSK699 (**G**) in Rh30 cells. Data are presented as the mean ± SEM ($n = 3$; AUC ***, $P \leq 1.0e{-}03$). **H,** Relative growth was assessed by CellTiter-Glo for Rh28 cells with the treatment of BI-1347 ± sgTADA2B and SEL-120-34A ± sgTADA2B. Data are presented as the mean ± SEM ($n = 6$; AUC **, $P \leq 1.0e{-}02$). **I,** Line graph reveals mean subcutaneous tumor volume (mm^3) formed by Rh28_sgChr2.2 or Rh28_sgTADA2B cells after treatment with the CDK8 inhibitor SEL-120-34A. Data are presented as the mean ± SEM (n_sgChr2.2-vehicle = 12, n_sgChr2.2-SEL-120-34A = 11, n_sgTADA2B-vehicle = 12, n_sgTADA2B-SEL-120-34A-12; AUC *, $P \leq 5.0e{-}02$). ns, not significant.

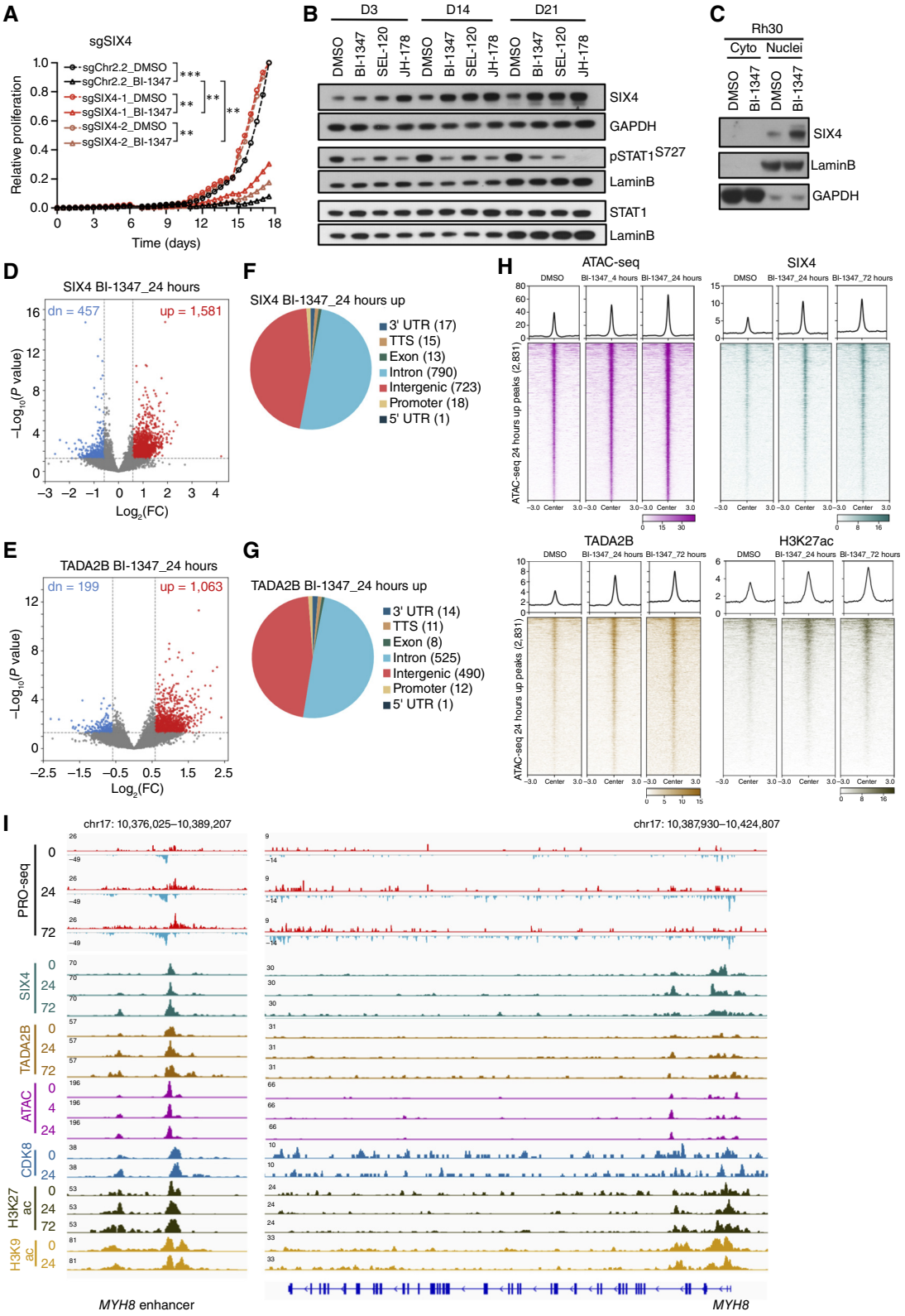


Figure 6. CDK8 inhibitor BI-1347 increases SIX4-driven gene expression involved in terminal muscle differentiation. **A,** Live-cell proliferation assay by Incucyte for BI-1347 treatment combined with CRISPR KO of *SIX4* with two different gRNAs. Data represent the means ± SEM ($n = 3$; AUC **, $P \leq 1.0e{-}02$; ***, $P \leq 1.0e{-}03$). **B,** Western blot analysis of SIX4 protein levels after treatment with three CDK8 inhibitors at indicated time points. Lamin B included as a loading control. **C,** Western blot analysis of SIX4 protein levels from cytoplasmic and nuclear fractions from Rh30 cells treated with DMSO or BI-1347 for 14 days. Lamin B and GAPDH served as nuclear and cytoplasmic loading controls, respectively. (*continued on following page*)

of genes associated with myogenic differentiation, such as *MYBPH*, *MYH8*, *MYL1*, *RUNX1*, and *VGLL2*. This aligns with findings in AML, in which CDK8 inhibition promoted cellular maturation, and in colon cancer, in which it induced differentiation (44). In the case of aRMS, both CDK8 inhibition and PAX3::FOXO1 degradation release the block on muscle differentiation imposed by PAX3::FOXO1, allowing aRMS cells to adopt a more differentiated phenotype. The transcriptional reprogramming influences the expression of genes involved in myogenic differentiation pathways and underpins the shift of aRMS cells from a proliferative state to a more differentiated state after CDK8 inhibition.

Previous studies report that PAX3::FOXO1 recruits transcriptional regulatory factors, including CDK8 and SMARCA4, and that CDK8 localization on chromatin is decreased with the reduced chromatin accessibility following rapid PAX3::FOXO1 degradation (8, 48). Whether these transcriptional regulatory factors are required for the chromatin binding of PAX3::FOXO1 broadly or its target sites are not well defined. Our data suggest that CDK8 inhibition does not broadly affect PAX3::FOXO1 chromatin occupancy or its transcriptional regulatory function. Even at the PAX3::FOXO1-controlled core enhancers, chromatin association of PAX3::FOXO1 and CDK8 remained intact. Notably, CDK8 inhibition selectively activated differentiation-related enhancers without affecting "stemness" transcription factors directly regulated by PAX3::FOXO1 at early time points. The transcriptional profiles induced by CDK8 inhibition and PAX3::FOXO1 degradation, however, showed partial overlap, particularly in the activation of myogenic differentiation genes at later time points, suggesting that the secondary effects of these perturbations are related. In addition, although the examination of PAX3::FOXO1 protein levels and its subcellular localization does not support a direct regulation of PAX3::FOXO1 by CDK8, we cannot rule out the possibility of phosphorylation of the fusion or other transcription factors by CDK8. In addition, the study of SMARCA4 suggests that the degradation of SMARCA4 also induces myogenic differentiation in aRMS (48). Whether Mediator and the BAF complex cooperate in PAX3::FOXO1 aRMS to regulate transcription remains to be determined.

Our genome-scale CRISPR BI-1347 anchor screen identified the critical role of the SAGA complex in mediating the transcriptional coactivation and differentiation-promoting effects of CDK8 inhibition in aRMS. Specifically, the identification of the KO of SAGA components *TADA2B* and *KAT2A* from the HAT module and *TAF5L* from the core module as key resistance hits in the genome-scale CRISPR–Cas9 screen highlights the essential collaboration between Mediator and SAGA in the regulation of differentiation-associated transcription. Disruption of these proteins attenuated both the transcriptional activation of differentiation-related enhancers at genes, such as *MYL1*, *RUNX1*, *SEMA3D*, and *VGLL2*, and growth inhibition induced by CDK8 inhibitors, suggesting that SAGA's HAT module facilitates the enhancer-driven transcriptional elongation required for muscle differentiation. Whereas at baseline, TADA2B is localized at both promoters and enhancers, the increased TADA2B with CDK8 inhibition was at sites with increased open chromatin at enhancers. These findings align with our observation of increased eRNA transcription and chromatin accessibility at differentiation-associated loci following CDK8 inhibition. Although the SAGA HAT module is required for H3K9 acetylation, there is no notable H3K9ac increase at sites which gain TADA2B binding. As the H3K9ac mark is more heavily involved in promoter activity, and the sites with gain of TADA2B binding are mostly enhancer sites, it is likely that H3K27ac function is more critical at these sites than H3K9ac for gene activation.

The CRISPR screen also identified a muscle development–related transcription factor needed for the full activity of BI-1347. SIX4 and other SIX family member proteins play an essential role in several stages of skeletal muscle development. Whereas SIX1 is reported to repress RMS differentiation, SIX4 is reported to promote the early specification of hypaxial myogenic progenitors through transactivation of PAX3, while later controlling myoblast determination and differentiation via activation of *MYF4*, *MYOD1*, *MYF6*, and *MYOG* (34, 49–51). In aRMS, in which PAX3::FOXO1 enforces an undifferentiated state, our findings suggest that the CDK8 inhibitor BI-1347 disrupts this oncogenic program in part by inducing a differentiation permissive transcriptional landscape, leading to the activation of SIX4-driven muscle differentiation programs. In our screen, other upregulated muscle differentiation–related genes, such as *MYH8*, *MYL1*, *RUNX1*, *SEMA3D*, and *VGLL2*, do not score as rendering resistance to BI-1347 when knocked out, suggesting they may act as downstream targets of the SIX4-induced myogenic differentiation transcriptional cascade rather than the upstream node.

Although there is a strong correlation between aRMS dependency on *CDK8* by CRISPR KO and the response to CDK8 chemical inhibition, we noted that pharmacologic inhibition of CDK8 resulted in more dynamic transcriptional changes compared with genetic KO. One possibility is that the activity of the CDK8 small-molecule inhibitors is enhanced by their dual effect on CDK19, a paralog of CDK8. Going against this hypothesis, our analysis of the DepMap dataset indicates that CDK19 is not a dependency in aRMS cell lines, and *CDK19* KO does not score in our CRISPR CDK8 inhibitor anchor screen as either a dependency or as a sensitizer. Nevertheless, simultaneous KO of both *CDK8* and *CDK19* would need to be assessed to rigorously rule out this possibility.

The BI-1347 CRISPR modifier screen, however, did identify that KO of Mediator kinase members rendered partial resistance to BI-1347. We next determined that there is a

Figure 6. ***(Continued)*** **D** and **E,** Volcano plots showing LFC of SIX4 (**D**) and TADA2B (**E**) genome binding sites determined by CUT&RUN analysis. Red highlights significantly upregulated sites, and blue highlights significantly downregulated sites (LFC 1.5, P adj < 0.05). **F** and **G,** Pie charts showing the annotation of upregulated CUT&RUN peaks for SIX4 (**F**) and TADA2B (**G**) sites after 24 hours of BI-1347 treatment in Rh30 cells. **H,** Heatmaps of time course analysis of ATAC-seq, SIX4, TADA2B, and H3K27ac signal around upregulated ATAC-seq peaks at 24 hours of BI-1347 treatment. **I,** IGV gene tracks showing the PRO-seq, SIX4, TADA2B, ATAC-seq, CDK8, H3K4me3, H3K27ac, and H3K9ac at the *MYH8* gene body and enhancer loci at indicated time points of BI-1347 treatment. dn, downregulated; up, upregulated; UTR, untranslated region.

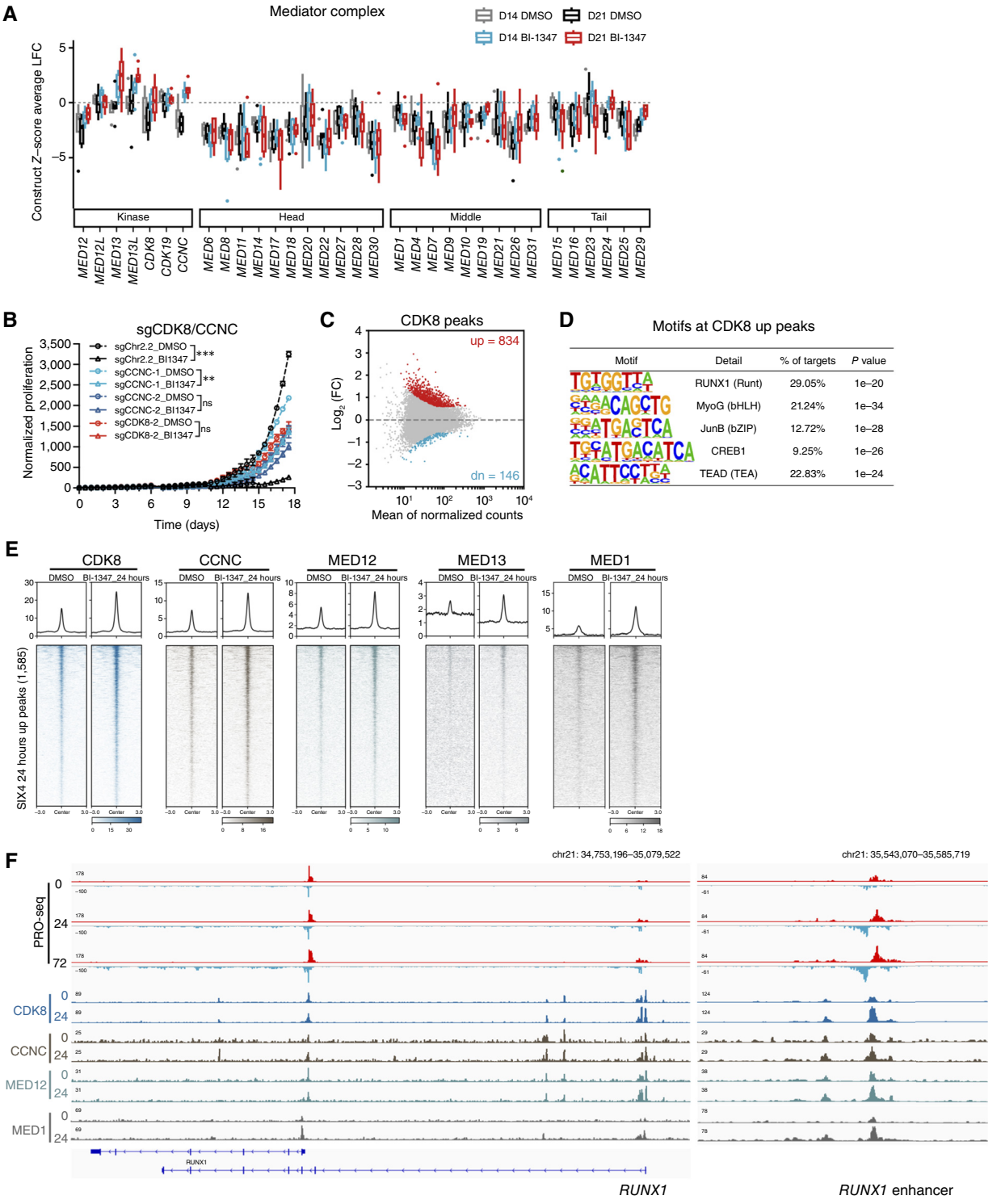


Figure 7. The Mediator kinase module is required for maximal CDK8 inhibitor activity. **A,** Box and whisker plots showing construct-level *Z*-score averages for individual genes in the Mediator complex from a genome-wide CRISPR–Cas9 screen in Rh30 cells treated with DMSO (gray/black) or BI-1347 (blue/red) for 14 days (gray and blue) or 21 days (black and red). Genes are grouped by Mediator functional modules. Boxes indicate the median and interquartile range (IQR; 25th–75th percentile); whiskers extend to 1.5× the IQR. Values beyond the end of the whiskers are plotted individually. **B,** Live-cell proliferation assessed by Incucyte for BI-1347 ± sgCCNC (blue) or sgCDK8 (red). Data represent the means ± SEM ($n = 3$; AUC **, $P \leq 1.0e{-}02$; ***, $P \geq 1.0e{-}03$). **C,** MA plot showing changes of CDK8 binding site assessed by CUT&RUN after 24 hours of BI-1347 treatment. Significantly increased CDK8 peaks are highlighted in red; significantly decreased CDK8 peaks are highlighted in blue (P adj < 0.05, FC >1.5 or < –1.5). **D,** Motif analysis of the regions with increased CDK8 DNA binding peaks from CUT&RUN analysis in Rh30 cells. **E,** Heatmaps showing chromatin occupancy of CDK8, CCNC, MED12, MED13, and MED1 at regions with upregulated SIX4 binding at 24 hours of DMSO or BI-1347 treatment. **F,** IGV gene tracks showing the PRO-seq, CDK8, CCNC, MED12, and MED1 binding at the *RUNX1* gene body and enhancer loci at indicated time points after BI-1347 treatment. dn, downregulated; up, upregulated.

gain of binding at specific sites on chromatin of Mediator kinase module members, such as CDK8, CCNC, MED12, and MED13, particularly at the sites in which SIX4 and the SAGA complex are also gained with CDK8 inhibitor treatment in aRMS cells. In addition to the Mediator kinase module, we determined that MED1, a member of the Mediator middle module, is also increased at sites with gain of Mediator kinase module binding. All told, these results support the hypothesis that BI-1347 may have both a loss-of-function (inhibition of CDK8 enzymatic activity) and gain-of-function (inhibitor trapping) effect on Mediator-regulated transcription, which will be the focus of our future studies. Kinase inhibitor trapping has been observed in other studies. For example, structural analyses showed that imatinib becomes stably entrapped within the ABL kinase, and a similar kinase trapping mechanism has been reported for a p38α kinase inhibitor, resulting in enhanced compound affinity (52). Similarly, PARP inhibitors work in part by trapping PARP at sites of DNA damage preventing its repair (53). Here, our data suggest that CDK8 inhibition and the trapping of inhibited mediator kinase enhances the activity of the mediator complex.

Induction of myogenic differentiation in aRMS by the CDK8 inhibitor BI-1347 suggests that CDK8 inhibitors may serve as modulators to counteract aRMS oncogenic activity. By disrupting the repressive transcriptional network maintained by PAX3::FOXO1 and inducing the activated transcriptional network maintained by other transcription factors such as SIX4, CDK8 inhibitors can restore differentiation programs, offering a novel therapeutic strategy for aRMS. Indeed, the use of differentiation therapy has expanded in recent years with the FDA approval of IDH and menin inhibitors for the treatment of AML (54, 55).

In considering the translation of CDK8 inhibition to the clinic, early safety concerns were raised as the *Cdk8*$^{-/-}$ mouse is embryonic lethal with failure of compaction of embryonic blastomeres (56). CDK8, however, is not essential for cell growth or survival of *Drosophila* S2 cells or 293T cells, and systemic inducible *Cdk8* KO mice have no survival defect (56–58). Encouragingly, *Cdk8* inhibitors such as SEL-120-34A have shown promise in preclinical studies and are currently in clinical trials for treatment of advanced AML and high-risk MDS (https://clinicaltrials.gov). In considering clinical translation, one must also consider subsets of patients most likely to respond. Our data suggest that *CDK8* is a strong dependency in aRMS cells expressing PAX3::FOXO1. In contrast, the PAX7::FOXO1-positive model CW9019 was largely insensitive. Retrospective analyses of clinical data indicate that PAX7::FOXO1 portends a more favorable prognosis than the PAX3::FOXO1 fusion (59), supporting biological differences between these two molecular subtypes. Only one PAX7::FOXO1 cell line was available to us; thus, more models of this subset will be needed to thoroughly address this question. Finally, it is important to note that drug combinations will likely be needed with CDK8 inhibitors to achieve maximal antitumor activity and regression of aRMS tumors.

In summary, our findings highlight the potential of CDK8 inhibitors as differentiation-inducing agents in aRMS and reveal new insights about the mechanistic role of CDK8 in this disease.

METHODS

Material Availability

All the materials generated in this study are accessible upon request.

Cell Lines

The Rh28, JR, CW9019, RD, and SMSCTR cell lines were cultured in RPMI-1640 (Corning by Mediatech, Inc.) containing 10% FBS (Sigma-Aldrich). Rh30, Rh4, RHJT, and HEK293T cell lines were cultured in DMEM (Corning by Mediatech, Inc.) containing 10% FBS (Sigma-Aldrich). The Rh30_PAX3::FOXO1-FKBP-HA engineered line was cultured in RPMI-1640 (Corning by Mediatech, Inc.) containing 10% FBS (Sigma-Aldrich) and was generously provided by Dr. Scott Hiebert at Vanderbilt University. The SkMC cell line was cultured in skeletal muscle cell growth media (PromoCell) with 5% FBS (Sigma-Aldrich). All cell lines consistently tested *Mycoplasma*-negative (MycoAlert, Lonza) and were confirmed to have the correct identities by short tandem repeats profiling.

Small-Molecule Inhibitors

BI-1347 and BI-1374 were generously provided by Boehringer Ingelheim through OpnMe.com. SEL-120-34A was purchased from Selleckchem (#S8840) and Adooq (#A21485). JH-XII-178 was generously provided by Dr. John Hatcher and Dr. Nathanael Gray. GSK699 was synthesized by WuXi AppTec.

shRNAs

The shRNA was cloned into pLKO.1-puro (Addgene, plasmid #8453) and Tet-pLKO-puro (Addgene, plasmid #21915).

shNT: CCGGCAACAAGATGAAGAGCACCAACTCGAGTTGGTG CTCTTCATCTTGTTG TTTTTG.
shCDK8-1: CCGGATGTCCAGTAGCCAAGTTCCACTCGAGTGG AACTTGGCTACTGGACATTTTTT.
shCDK8-2: CCGGCGAGAGCTTAAGCATCCAAACCTCGAGGTT TGGATGCTTAAGCTCTCGTTTTTTG.

sgRNAs

The sgRNA was cloned into lentiCRISPR v2 containing Cas9 and puromycin resistance marker plasmid (Addgene, plasmid #52961).

sgChr2.2: GGTGTGCGTATGAAGCAGTG.
sgCDK8-2: CAGCAATTCACCTTACCCAG.
sgCDK8-3: GAGGACCTGTTTGAATACGA.
sgCDK8-4: AGTGACTTCACCATTCCCCG.
sgTADA2B-1: GACAGGTGTGGTCTGTCACG.
sgTADA2B-3: GGGCGGCTGGACCAGTCGCG.
sgTAF5L-1: AAACAGTCCGAAGAGCACAG.
sgTAF5L-3: GCAGAAACATTCCATGGAAG.
sgSIX4-1: GCCTGCCCAGAAGTTCCGAG.
sgSIX4-2: GGATCAGGTACAACTCCACT.
sgCCNC-1: ACATGTTGCTTCCCCTTGCA.
sgCCNC-2: GATGCCAAAAACACACATGT.

Western Blotting

Cells were collected at indicated time points and lysed with RIPA buffer (50 nmol/L Tris, pH 8.0, 150 mmol/L NaCl, 1% NP-40, 0.5% sodium deoxycholate, and 0.1% SDS) containing protease inhibitors (aprotinin, Sigma-Aldrich #6279; phenylmethanesulfonyl fluoride solution, Sigma-Aldrich #93482; Phosphatase Inhibitor Cocktail 3, Sigma-Aldrich #P0044). Lysates were sonicated, cleared by centrifugation, subjected to NuPAGE Tris-Acetate protein gels to separate proteins (Thermo Fisher Scientific, #EA03785BOX),

and then subjected to electrophoretic transfer to membranes. The primary antibodies used in this study include: CDK8 (ProteinTech, #22067; Cell Signaling Technology, #4106S; Santa Cruz Biotechnology, #SC-13155; Abcam, #ab229192), STAT1 (Cell Signaling Technology, #9176S), pSTAT1S727 (Cell Signaling Technology, #8826S), SIX4 (Santa Cruz Biotechnology, #SC-390779), GAPDH (Santa Cruz Biotechnology, #SC-365062), LaminB (Abcam, #ab16048; Santa Cruz Biotechnology, #SC-374015), ACTB (Sigma-Aldrich, #A2066), total PARP (Cell Signaling Technology, #9542S), cleaved PARP (Cell Signaling Technology, #5625S), CC3 (Cell Signaling Technology, #9664S), FOXO1 (Cell Signaling Technology, #2380S), PAX3::-FOXO1 (CancerTools, #160866), MYC (EMD Milipore, #05-724), streptavidin–horseradish peroxidase (HRP; Cell Signaling Technology, #3999), TAF5L (ProteinTech, #19274), TADA2B (ProteinTech, #17367), KAT2A (ProteinTech, #66575), KAT2B (Cell Signaling Technology, #C14G9), CCNC (ProteinTech, #26464), MED13 (ProteinTech, #26464), MED12 (ProteinTech, #20028), MED1 (Bethyl Laboratories, #A300-793A), MEF2C (Abcam, #ab221493), RUNX1 (ProteinTech, #25315), MYL1 (ProteinTech, #15814), MF20 (Thermo Fisher Scientific, #MAB4470), and FLAG (Sigma-Aldrich, #F3165). Signal was visualized with secondary HRP-linked antibodies (Cell Signaling Technology, #7074S; Cell Signaling Technology, #7076S) using the Licor Odyssey imaging system or IRDye-conjugated antibodies (Fisher Scientific, #NC0250902; Thermo Fisher Scientific, #NC0250903) using enhanced chemiluminescence Western blot substrates (Thermo Fisher Scientific, #54002401) on X-ray film (Life Technologies, #34089).

Cell Growth Assays

Trypan Blue Exclusion Assay. Cells were transduced with shNT, shCDK8-1, or shCDK8-2 and seeded at 2×10^5 cells/well after puromycin selection (3 days of antibiotic selection). Cells were then stained with Trypan Blue solution (Sigma-Aldrich, #T8154) followed by automated cell counting on a hematocytometer (Bio-Rad TC20 automated cell counter). Viable cells were counted with Trypan Blue dye exclusion every day for 4 days. Quantification was performed in triplicate, and the values averaged and shown with standard deviations. On-target editing of the shRNA was confirmed by Western blot.

CellTiter-Glo Cell Viability Assay. Cells were treated with indicated-small molecule inhibitors or were transfected with indicated sgRNAs and seeded into 384-well plates at 800 cells/well. The CellTiter-Glo Luminescent assay (Promega, #G7573) was performed according to the manufacturer's instructions. Each condition included at least six replicates, and each experiment was performed in triplicate. On-target editing of the CRISPR guides and small-molecule inhibitors was confirmed by Western blot.

Incucyte Live-Cell Proliferation Assay. Cells with indicated sgRNA transduction, small-molecule inhibitor treatment, or combination were seeded in 96-well plates at 2,000 cells/well and allowed to adhere overnight. Images were captured every 12 hours over the course of the experiment using phase-contrast imaging. Confluence was quantified using the Incucyte integrated analysis software, and proliferation curves were generated based on percent confluence over time. All conditions were assessed in technical triplicates and normalized to control treatments as appropriate.

In Vivo Xenograft Tumor Experiments

Rh28 cells with CDK8-targeting shRNAs, sgChr2.2 and sgTADA2B-3, or Rh30 cells were harvested, counted, and resuspended in 70% media and 30% Matrigel (Corning, #354234). A total of 3×10^6 Rh28_sgChr2.2/sgTADA2B cells, 1×10^7 Rh30 cells, and Rh28_tet-shCDK8 cells were subcutaneously injected into the flanks of Fox Chase SCID Beige mice (Charles River Laboratories, #250). To induce shRNA expression, mice were fed with doxycycline-containing chow (Envigo, #TD.01306) starting on the day of established tumors (~100 mm^3). For Rh30 SEL-120-34A study, SEL-120-34A was purchased from SelleckChemicals (#S8840, batch#S884001) and dissolved in H_2O. Mice were treated with SEL120-34A by oral gavage at 60 mg/kg daily (5 days on and 2 days off for 19 days in total). For Rh28_sgChr2.2/sgTADA2B-3 CDK8 inhibitor SEL-120-34A study, SEL-120-34A was purchased from AdooQ Bioscience (#A21485, batch#L21485B002) and dissolved in H_2O. Mice were treated with SEL-120-34A by oral gavage at 60 mg/kg daily (14 days on and 2 days off and then 5 days on for 19 doses over 21 days). Animal weight was monitored, and tumor size was measured two times a week using digital calipers. Mice were euthanized at humane endpoint, and tumors were collected for downstream analysis. Duke University School of Medicine and Dana-Farber Cancer Institute (DFCI) institutional animal care and use committees (IACUC) have approved these studies, and all animal procedures were performed in accordance with institutional IACUC guidelines.

Hematoxylin and Eosin Staining and Immunohistochemistry

Xenograft tumors were fixed in 10% formalin/70% ethanol and processed by the Duke University BioRepository & Precision Pathology Center, including embedding in standard paraffin blocks. Five-micrometer sections of formalin-fixed, paraffin-embedded xenograft tumors tissue were deparaffinized in xylene, rehydrated through a graded series of ethanol, and rinsed in distilled water. Slides were stained with hematoxylin to visualize nuclei, followed by differentiation in acid alcohol and bluing in ammonium hydroxide. Eosin was then applied to counterstain cytoplasmic and extracellular components. After dehydration and clearing, sections were mounted with coverslips and visualized under a light microscope.

For CC3 staining of tumor sections, 5-μm sections were stained using the rabbit monoclonal CC3 antibody (Cell Signaling Technology, #9661S, RRID: AB_2341188) at 1:400, with Antibody Diluent (Discovery, #760-108). Staining was performed using the Ultra Discovery automated platform. Sections were pretreated (epitope retrieval) with cell conditioning solution CC1 (Roche, #950-124) for 56 minutes. CC3 antibody was applied and incubated for 60 minutes at 36°C. Rabbit IgG, substituted for the primary antibody, was used as the negative control. After binding of the primary antibody, anti-rabbit HQ (Roche, #760-4815) was applied and incubated for 12 minutes, followed by 12-minute incubation with anti-HQ HRP. For visualization, ChromoMap DAB (Discovery, #760-159) was applied and incubated for 5 minutes. Slides were counterstained with hematoxylin. Images were captured by a pathologist (R.C. Bentley), and then four sections were quantitated for positive and negative staining in a blinded fashion using ImageJ.

For CDK8 staining of RMS PDX tissue, a rhabdomyosarcoma PDX microarray was obtained from the Childhood Solid Tumor Network at St. Jude Children's Research Hospital (60), courtesy of Dr. Elizabeth Stewart. The microarray was deparaffinized, rehydrated, and subjected to antigen retrieval in antigen unmasking buffer (Vector Labs, #H-3300). Endogenous peroxidase activity was blocked with 3% hydrogen peroxide, followed by 30-minute blocking buffer incubation at room temperature. Sections were incubated overnight at 4°C with an anti-CDK8 primary antibody (Santa Cruz, #sc-13155), followed by a biotinylated secondary antibody (Vector Labs, #PK-6200) and detection using a DAB chromogen kit (Vector Labs, #SK-4100). Slides were counterstained with hematoxylin (Sigma-Aldrich, #MHS16), dehydrated, mounted, and imaged.

Cell-Cycle Analysis

Cells were treated with DMSO or BI-1347 for 3, 7, 14, and 21 days, pulsed with 20 mmol/L bromo-2′-deoxyuridine (BrdU) for 2 hours, and fixed overnight with 70% ethanol at 4°C. After staining with fluorescein isothiocyanate (FITC)-conjugated anti-BrdU (BD Biosciences, #556028) and counterstaining with 7-aminoactinomycinD (7-AAD) (BD Biosciences, #559925), cells were analyzed by flow cytometry. All flow cytometry figures were generated using FlowJo software (v10.9).

Apoptosis Analysis

Annexin V Assay. Cells were treated with DMSO or BI-1347 for 3, 7, 14, and 21 days, and 1×10^5 cells were collected for FITC-conjugated Annexin V and propidium iodide staining (BD Biosciences, #556547). Cells were analyzed by flow cytometry. All flow cytometry figures were generated using FlowJo software (v10.9).

Caspase-Glo 3/7 Assay. Cells were transduced with shNT, shCDK8-1, or shCDK8-2, and cells were seeded at 2×10^4 cells/well in 96-well plate after 3 days of antibiotic selection. After 4 days, 10 μL of Caspase-Glo reagent was added to each well, and plates were incubated at room temperature for 30 minutes before measuring luminescent signal. Each condition includes at least six replicates, and each experiment performed in a minimum of triplicate.

Immunofluorescence

Cells were seeded on coverslips and treated with DMSO or BI-1347 for 7 days. After fixation using 3.7% paraformaldehyde for 15 minutes at room temperature, the cells were permeabilized using 0.3% Triton X-100 for 30 minutes. Cells were blocked with 1% bovine serum albumin (BSA) in PBS for 30 minutes in a humidified chamber and then incubated with primary MF20 antibody (Thermo Fisher Scientific, #MAB4470) diluted in blocking buffer containing 0.5% NP-40 for 1 hour at 37°C. After PBS washing three times, cells were incubated in Alexa Fluor secondary antibody (Abcam #ab150117, Invitrogen A-11034) with phalloidin (Thermo Fisher Scientific, #A12380) and 4′,6-diamidino-2-phenylindole (DAPI) diluted in blocking buffer containing 0.5% NP-40 in PBS at 37°C for 45 minutes. Coverslips were mounted on slides with ProLong Gold Antifade reagent (Thermo Fisher Scientific, #P36930) and dried overnight in the dark. Images were collected using a Nikon fluorescence microscope.

Real-time PCR Assay

For TaqMan Real-Time PCR assays, cells with indicated treatments were collected, and total RNA was extracted using TRIzol reagent (Life Technologies, #15596026) and reverse-transcribed into cDNA using the High-Capacity cDNA Reverse Transcription Kit (Life Technologies, #1708891). Real-time PCR reactions were carried out in 384-well plates using TaqMan Universal PCR Master Mix (Life Technologies, #4374338) on a QuantStudio 6 Flex Real-Time PCR System under standard cycling conditions. All reactions were run in six technical replicates, and relative expression was normalized to control samples. For SYBR Green Real-Time PCR assays, cells were similarly extracted but reverse-transcribed into cDNA using the iScript cDNA Synthesis Kit (Bio-Rad, #1708891), with real-time PCR reactions carried out in 96-well plates using SsoAdvanced Universal SYBR Green Supermix (Bio-Rad, #1725271) on a CFX Connect Real-Time PCR Detection System (Bio-Rad) under standard cycling conditions, reactions run in three technical replicates, and relative expression normalized to control samples. For both methods, gene expression was quantified using the ΔΔCt method, with GAPDH as an internal control.

TaqMan Probes in This Study

GAPDH: Life Technologies, #Hs02786624_g1.
RUNX1: Life Technologies, #Hs02558380_m1.
SEMA3D: Life Technologies, #Hs00380877_m1.
VGLL2: Life Technologies, #Hs00403461_m1.
MYL1: Life Technologies, # Hs00984899_m1.

SYBR Primers in This Study

GAPDH:
Forward: 5′ TGGAGAAGGCTGGGGCTCATT 3′.
Reverse: 5′ AAGCAGTTGGTGGTGCAGGAG 3′.
CDK8:
Forward: 5′ AAG CTG CTT ACC ATG GAC CC 3′.
Reverse: 5′ GCT GCT GGT TCT TTT TGT CTC C 3′.
Myoglobin:
Forward: 5′ AGT CGC ATG CCA CCA AGC ACA A 3′.
Reverse: 5′ CCT GGG CAT CAG CAC CAA AGT C 3′.

PRO-seq and Data Processing

PRO-seq was performed in biological replicates as previously described using 10 million cells treated with DMSO or BI-1347 for 4, 24, and 72 hours (61). After washing and permeabilization, nuclei were stored in freezing buffer and then subject to biotin run-on using biotin-11-ATP, biotin-11-GTP, biotin-11-CTP, and biotin-11-UTP [PerkinElmer, #NEL54(2, 3, 4, 5)001]. RNA was reversed-transcribed and amplified to make the cDNA library for sequencing by the Harvard Medical School Nascent Transcriptomics Core. The sequences were aligned to hg38 using bowtie2 before using the Nascent RNA Sequencing Analysis pipeline (28) to determine the gene body and eRNA changes.

ssGSEA of DepMap CRISPR Screening Data

Genome-wide CRISPR–Cas9 loss-of-function dependency data were obtained from the DepMap Public 24Q2 release (http://depmap.org). The gene-effect matrix containing Chronos-corrected dependency scores for all screened genes across all cell lines was used as input. Prior to analysis, common essential genes and genes with more than 100 missing (i.e., not available, "NA") Chronos scores were excluded to reduce noise and improve statistical robustness. Differential dependency analysis was first performed to identify genome-wide, lineage-specific gene-level effect size differences by comparing each lineage against all nonlineage cell lines. This analysis used the moderated *t* test with empirical Bayes variance shrinkage implemented in the *limma* R package (Bioconductor v3.22; ref. 62). Significance thresholds followed DepMap recommendations: effect size < −0.25 and q value < 0.10. The empirical Bayes correction was particularly important for stabilizing variance estimates in lineages represented by few models, such as aRMS, which includes only eight cell lines. This analysis identified 75 genes with significant lineage-specific dependencies in aRMS, with CDK8 ranking 52nd (effect size = −0.30; adjusted *P* value = 0.04). We next extended the differential dependency analysis to the protein-complex level by evaluating genome-wide lineage-specific dependency profiles for coordinated functional vulnerabilities across the comprehensive collection of experimentally validated mammalian protein complexes in the CORUM v4.1 database (16, 63, 64). Complex-level dependency patterns were assessed using ssGSEA implemented with the *fgsea* R package (Bioconductor v3.22, bioRxiv 060012). ssGSEA is established as an enrichment analysis able to identify groups of coordinated genes that together cooperate to score as a significant group hit, even if the contribution of individual gene members is weaker. For each lineage-versus-background comparison, *fgsea* was applied to the lineage-specific ranked effect size vector to compute normalized enrichment scores (NES) for each CORUM complex, reflecting the degree to which the complex

members were coordinately enriched among top-ranked dependencies. Significance thresholds for protein-complex dependencies were set at NES < −1.5 and *P* value < 0.10. Several ARC/Mediator protein complexes containing CDK8 emerged as top enriched dependency hits for the aRMS lineage. As an orthogonal validation, a simple hypergeometric test based overlapping analysis for the 75 aRMS-specific gene dependencies with CORUM protein complexes similarly identified CDK8-containing complexes among the most significantly enriched hits.

RNA-seq and Data Processing

All RNA-seq experiments were performed in biological triplicate. Cells with the indicated treatments were collected, and total RNA was extracted using TRIzol reagent. RNA was submitted to Novogene for library preparation and sequencing. Gene expression values were derived from paired-end RNA-seq data. The RNA-seq processing pipeline was roughly modeled on the GTEx pipeline (https://github.com/broadinstitute/gtex-pipeline/). FastQC was used to evaluate read quality on raw RNA-seq reads. Reads were aligned to the human genome (hg38) using STAR (v2.7.2b). Transcript-level quantifications were calculated using RSEM (v1.3.1). Gene counts from STAR were then used to quantify differentially expressed genes between the experimental and control conditions using the R Bioconductor package DESeq2 (65) using the approximate posterior estimation for Generalized Linear Model (GLM) coefficients (apeglm) method for effect size. Normalized expression values for individual samples were obtained from RSEM $\log_2$ TPM values with the RSEM $\log_2$(TPM + 1) values used for GSEA and producing RNA-seq heat map plots.

CUT&RUN and Data Processing

CUT&RUN experiments were performed in biological duplicate as described (66). In brief, 250,000 cells with the indicated treatments were collected and incubated with CUTANA concanavalin A–conjugated paramagnetic beads (EpiCypher, #21-1401) for 10 minutes at room temperature. Cells were permeabilized using 0.02% freshly dissolved digitonin (Sigma-Aldrich, #300410) and then subject to primary antibody incubation at 4°C overnight. Primary antibodies used for CUT&RUN in this study include the following: CDK8 (ProteinTech, #22067), SIX4 (Santa Cruz Biotechnology, #SC-390779), HA (Cell Signaling Technology, #C29F4-3724), TADA2B (ProteinTech, #17367), CCNC (ProteinTech, #26464), MED13 (ProteinTech, #26464), MED12 (ProteinTech, #20028), MED1 (BETHYL, #A300-793A), H3K9ac (Cell Signaling Technology, #9649S), H3K4me3 (EpiCypher, #13-0041), and H3K27ac (Cell Signaling Technology, #8173S). Following washing, targeted regions of the genome were digested using CUTANA pAG-MNase (EpiCypher, #15-1116) fusion protein with 2-hour incubation on ice. DNA was then extracted using Monarch PCR and DNA Cleanup Kit (New England Biolabs, #T1030S), and the sequencing libraries were generated using the NEBNext Ultra II DNA Library Prep Kit (New England Biolabs, #E7654L) and NEBNext Multiplex Oligos for Illumina 96 Unique Dual Index Primer Pairs (New England Biolabs, #E6440S). Sequencing was performed by the Molecular Biology Core Facilities (MBCF) at DFCI.

Sequencing read quality was examined using FastQC (http://www.bioinformatics.babraham.ac.uk; v0.11.9). Raw FASTQ data were trimmed using Trimmomatic v0.38, and paired-end reads were aligned to human hg38 genome using Bowtie2 (v2.3.5) in very sensitive local mode (--phred33 -I 0 -X 2000 -N 1 --very-sensitive). Peaks were called using MACS2 (v2.1.4) with a threshold of q < 0.01, and peaks were annotated to the nearest TSS using HOMER. Differential analysis was performed using DiffBind and DESeq2. Significantly changed peaks were defined by a 1.5-fold change threshold and false discovery rate (FDR) < 0.05. Bigwig files were normalized and generated using Deeptools. Heatmaps were created by Deeptools using the normalized bigwig files.

ATAC-seq and Data Processing

ATAC-seq was performed in biological triplicate following the manufacturer's protocol (Active Motif, #53150). A total of 100,000 cells with indicated treatment were used to isolate nuclei. Nuclei were incubated with Tagmentation Master Mix at 37°C for 30 minutes after lysing the cells in ice-cold ATAC Lysis Buffer, and the DNA was purified with the DNA purification column. PCR amplification of tagmented DNA was performed to make libraries with the appropriate indexed primers. After SPRI bead clean-up, the DNA libraries were submitted to the MBCF at DFCI for sequencing.

Raw FASTQ data were trimmed by Trimmomatic v0.39, and paired end reads were aligned to a concatenated human genome hg38 using Bowtie2 (v2.3.5; --phred33 -I 0 -X 2000 -N 1 --very-sensitive). Peaks were called using Genrich (v0.6.1; https://github.com/jsh58/Genrich) with the following options: -j -y -r -e chrM -q 0.05 -a 20. Peaks were annotated to the nearest TSS using HOMER. Differential analysis was performed using DiffBind and DESeq2. Significantly changed peaks were defined by a 1.5-fold change threshold and FDR < 0.05. Bigwig files were generated and normalized using the DESeq2 size factors using Deeptools. Heatmaps were created by Deeptools using the normalized bigwig files.

Bio-ID Labeling and Mass Spectrometry

For each replicate, approximately 7×10^6 cells were transfected using FuGENE 6 (Promega) transfection reagent as according to the manufacturer's protocol and grown in DMEM. Forty-eight hours later, biotin was added to the cultures at 50 μmol/L and cultured for an additional 16 hours. Each replicate was lysed in 200 μL RIPA supplemented with cOmplete protease inhibitors (Roche), rotated end-over-end for 30 minutes, and cleared by centrifugation at 4°C. MydOne streptavidin-coated agarose beads (Invitrogen) were simultaneously equilibrated in RIPA buffer. Ninety percent of lysate was then added to the beads and rotated end-over-end for 16 hours at 4°C. The remaining 10% was used as input. Beads were then washed five times in wash buffer [0.5% (w/v) sodium deoxycholate, 0.5% (w/v) IGEPAL CA-630, 1 mmol/L Ethylenediaminetetraacetic acid (EDTA), 100 mmol/L NaCl, and 50 mmol/L Tris.Cl, pH 7.5] by end-over-end incubation for 5 minutes at 4°C. After final wash, beads were resuspended in 40 μL PBS + 2.5 μmol/L Biotin, and 10 μL 5× SDS Page loading buffer. Forty microliters of each sample were loaded onto an Invitrogen NuPAGE 4% to 12% SDS-PAGE gel and run for approximately 5 minutes to electrophorese all proteins into the gel matrix. The entire MW range was then excised in a single gel-band and subjected to standardized in-gel reduction, alkylation, and tryptic digestion. Following lyophilization of the extracted peptide mixtures, samples were resuspended in 20 μL of 2% acetonitrile/1% trifluoroacetic acid supplemented with 12.5 fmol/μL yeast ADH. From each sample, 3 μL was removed to create a quality control pool sample which was run periodically throughout the acquisition period.

Quantitative LC–MS/MS was performed on 4 μL of each sample using a nanoAcquity UPLC system (Waters Corp.) coupled to a Thermo QExactive HF-X high resolution accurate mass tandem mass spectrometer (Thermo Fisher Scientific) via a nanoelectrospray ionization source. Briefly, the sample was first trapped on a Symmetry C18 20 mm × 180 μm trapping column (5 μL/minute at 99.9/0.1 v/v water/acetonitrile), after which the analytical separation was performed using a 1.8 μm Acquity HSS T3 C18 75 μm × 250 mm column (Waters Corp.) with a 90-minute linear gradient of 5% to 30% acetonitrile with 0.1% formic acid at a flow rate of 400 nL/minute with a column temperature of 55°C. Data collection on the QExactive HF mass spectrometer was performed in a data-dependent acquisition mode of acquisition with a r = 120,000 (@ m/z 200) full mass spectrometry (MS) scan from m/z 375 to 1,600 with a target AGC value of 3e6 ions followed by 30 MS/MS scans at r = 15,000 (@ m/z 200) at a target AGC value of 5e4 ions and 45 milliseconds. A 20-second

dynamic exclusion was used to increase depth of coverage. The total analysis cycle time for each sample injection was approximately 2 hours. Following UPLC-MS/MS analyses, data were imported into Rosetta Elucidator v4.0 (Rosetta Biosoftware, Inc.), and analyses were aligned based on the accurate mass and retention time of detected ions ("features") using PeakTeller algorithm in Elucidator. Relative peptide abundance was calculated based on the area under the curve of the selected ion chromatograms of the aligned features across all runs. The MS/MS data were searched against the SwissProt *Homo sapiens* database (downloaded in August 2017) with additional proteins, including yeast ADH1, BSA, as well as an equal number of reversed-sequence "decoys") FDR determination. Mascot Distiller and Mascot Server were utilized to produce fragment ion spectra and perform the database searches. Database search parameters included fixed modification on Cys (carbamidomethyl) and variable modifications on Meth (oxidation) and Asn and Gln (deamidation). After individual peptide scoring using the PeptideProphet algorithm in Elucidator, the data were annotated at a 0.8% peptide FDR.

CRISPR–Cas9 Drug Modifier Screen and Data Processing

A genome-wide CRISPR–Cas9 loss-of-function screen was performed in Rh30 cells treated with a sublethal concentration (~IC_{50}) of CDK8 inhibitor BI-1347 to identify genetic modifiers of sensitivity or resistance to BI-1347 response. Cells stably expressing Cas9-mCherry were transduced with the genome-wide sgRNA library Avana-4 in duplicate at a low multiplicity of infection (~ 0.3) to ensure single sgRNA integration per cell, followed by puromycin selection. After recovery, cells were split into two arms and treated with either DMSO or BI-1347 at a concentration sufficient to induce partial growth inhibition (10 nmol/L) for 21 days. Cells were collected at days 14 and 21, and genomic DNA was extracted (Takara Bio #740950.50). Genomic DNA was submitted to the Broad Institute Genetic Perturbation Platform (GPP) for PCR-amplification and sequencing. sgRNA representation and gene-level enrichment were analyzed using the Broad Institute's GPP APRON analysis tool (https://portals.broadinstitute.org/gppx/apron/screener/) to identify candidate genes whose loss sensitized or conferred resistance to BI-1347 treatment.

Data Availability

This article does not report original software for next-generation sequencing data analysis. Any code for analysis or data visualization will be shared upon request. All genomic datasets are available at Gene Expression Omnibus accession GSE303028.

Authors' Disclosures

S. Zhang reports grants from Alex's Lemonade Stand Foundation during the conduct of the study. C.F. Malone reports grants from the National Cancer Institute (NCI) during the conduct of the study and personal fees from InduPro outside the submitted work; in addition, C.F. Malone has a patent for bispecific antibodies pending to InduPro. M. Just reports grants from the National Institutes of Health (NIH) during the conduct of the study. B. Guedes reports grants from the NIH during the conduct of the study. K.C. Wood reports grants from the NIH during the conduct of the study, as well as nonfinancial support from Aurova Therapeutics, Celldom, and Decrypt Biomedicine, personal fees from Retroviral Therapeutics and Guidepoint Global, and personal fees and nonfinancial support from Stelexis Biomedicine outside the submitted work. C.M. Linardic reports grants from the NCI (U54 CA231630 and UM1 CA294108), CureSearch for Children's Cancer Foundation, Hyundai Hope on Wheels, Rally Foundation for Childhood Cancer Research, and St. Baldrick's Foundation and other support from Childhood Solid Tumor Network at St. Jude's Children's Research Hospital (tissue microarrays), Duke University BioRepositories & Precision Pathology Center, supported by P30 CA014236, and Duke University NICHD T32 HD094671 fellowship program during the conduct of the study; Dr. Linardic's laboratory received funding from Ryvu Therapeutics, her spouse is founder of Grid Therapeutics, LLC, a company developing therapeutic antibodies for lung cancer, and her family has stock in Thermo Fisher Scientific, Inc. and Laboratory Corp. of America. K. Stegmaier reports grants from the NCI during the conduct of the study, as well as other support from Auron Therapeutics and grants from DFCI/Novartis Drug Discovery Program outside the submitted work. No disclosures were reported by the other authors.

Authors' Contributions

S. Zhang: Conceptualization, data curation, formal analysis, funding acquisition, validation, investigation, visualization, methodology, writing–original draft, writing–review and editing. **K.L. Engel:** Validation, investigation, visualization. **A. Fahs:** Validation, investigation, writing–review and editing. **A. Jo:** Validation, visualization. **C.F. Malone:** Conceptualization, formal analysis, validation, investigation, visualization. **K.N. Ross:** Formal analysis, investigation, visualization. **M. Just:** Validation, investigation, visualization. **B. Guedes:** Validation, investigation, visualization. **D. Granum:** Validation, investigation, visualization. **K.M. Oristian:** Validation, investigation, visualization. **A.R. Kovach:** Validation, investigation, visualization. **G. Alexe:** Data curation, formal analysis, investigation, visualization. **G. DiGiovanni:** Validation, investigation, visualization. **L. Barbar:** Validation, investigation, visualization. **R.C. Bentley:** Validation, investigation, visualization. **C.G. Cerda-Smith:** Validation, investigation, visualization. **O. Le Roux:** Validation, investigation, visualization. **E.A. Mendes:** Validation, investigation, visualization. **S.P. Zimmerman:** Validation, investigation, visualization. **A. Taillon:** Validation, investigation, visualization. **V. Tong:** Validation, investigation, visualization. **A. Basanthakumar:** Validation, investigation, visualization. **M.G. Rees:** Data curation, software, methodology. **J.A. Roth:** Resources, data curation, software, supervision, methodology. **J.F. Shern:** Conceptualization, supervision. **K.C. Wood:** Conceptualization, supervision. **C.M. Counter:** Conceptualization, supervision. **C.M. Linardic:** Conceptualization, supervision, funding acquisition, writing–review and editing. **K. Stegmaier:** Conceptualization, supervision, funding acquisition, writing–review and editing.

Acknowledgments

This work was funded by awards from the NCI R35 CA283977 (K. Stegmaier), U54 CA231630 (C.M. Counter, C.M. Linardic, K.C. Wood), and UM1 CA294108 (C.M. Linardic); CureSearch for Children's Cancer Foundation; Hyundai Hope on Wheels; Rally Foundation for Childhood Cancer Research; St. Baldrick's Foundation (C.M. Linardic); Palumbo Rhabdomyosarcoma Research Fund (K. Stegmaier); and Corinne Cecilia Sciarappa Fund (K. Stegmaier). This work was also supported by the Pediatric Cancer Dependencies Accelerator of the Broad Institute, DFCI, and St. Jude Children's Research Hospital: peddep.org. S. Zhang was supported by an Alex's Lemonade Stand Fellowship (#22-27271). C.F. Malone was supported by the NIH under a Ruth L. Kirschstein National Research Service Award (F32CA243266). M. Just and B. Guedes were supported by NCI T32HD094671 fellowships. We thank the Duke University BioRepository & Precision Pathology Center (supported by P30CA014236) for assistance with tumor xenograft processing and staining and the Childhood Solid Tumor Network at St. Jude Children's Research Hospital for RMS PDX tissue microarrays.

Note

Supplementary data for this article are available at Cancer Discovery Online (http://cancerdiscovery.aacrjournals.org/).

Received July 5, 2025; revised May 1, 2026; accepted July 10, 2026; posted first July 14, 2026.

REFERENCES

1. Mitelman F, Johansson B, Mertens F. The impact of translocations and gene fusions on cancer causation. Nat Rev Cancer 2007;7:233–45. https://doi.org/10.1038/nrc2091.
2. Lobato MN, Metzler M, Drynan L, Forster A, Pannell R, Rabbitts TH. Modeling chromosomal translocations using conditional alleles to recapitulate initiating events in human leukemias. J Natl Cancer Inst Monogr 2008;2008(39):58–63. https://doi.org/10.1093/jncimonographs/lgn022.
3. Mertens F, Antonescu CR, Mitelman F. Gene fusions in soft tissue tumors: recurrent and overlapping pathogenetic themes. Genes Chromosomes Cancer 2016;55:291–310. https://doi.org/10.1002/gcc.22335.
4. Skapek SX, Ferrari A, Gupta AA, Lupo PJ, Butler E, Shipley J, et al. Rhabdomyosarcoma. Nat Rev Dis Primers 2019;5:1. https://doi.org/10.1038/s41572-018-0051-2.
5. Henley MJ, Koehler AN. Advances in targeting "undruggable" transcription factors with small molecules. Nat Rev Drug Discov 2021;20:669–88. https://doi.org/10.1038/s41573-021-00199-0.
6. Ognjanovic S, Linabery AM, Charbonneau B, Ross JA. Trends in childhood rhabdomyosarcoma incidence and survival in the United States, 1975–2005. Cancer 2009;115:4218–26. https://doi.org/10.1002/cncr.24465.
7. Ma X, Liu Y, Liu Y, Alexandrov LB, Edmonson MN, Gawad C, et al. Pan-cancer genome and transcriptome analyses of 1,699 paediatric leukaemias and solid tumours. Nature 2018;555:371–6. https://doi.org/10.1038/nature25795.
8. Zhang S, Wang J, Liu Q, McDonald WH, Bomber ML, Layden HM, et al. PAX3-FOXO1 coordinates enhancer architecture, eRNA transcription, and RNA polymerase pause release at select gene targets. Mol Cell 2022;82:4428–42.e7. https://doi.org/10.1016/j.molcel.2022.10.025.
9. Turco GM, Oberoi S, Ladle B, Raavi, Wagner L, Koehler AN, et al. Towards directed therapy for fusion-positive rhabdomyosarcoma. Pharmacol Ther 2025;276:108931. https://doi.org/10.1016/j.pharmthera.2025.108931.
10. Liu B, Liu X, Han L, Chen X, Wu X, Wu J, et al. BRD4-directed super-enhancer organization of transcription repression programs links to chemotherapeutic efficacy in breast cancer. Proc Natl Acad Sci U S A 2022;119:e2109133119. https://doi.org/10.1073/pnas.2109133119.
11. Gryder BE, Yohe ME, Chou HC, Zhang X, Marques J, Wachtel M, et al. PAX3-FOXO1 establishes myogenic super enhancers and confers BET bromodomain vulnerability. Cancer Discov 2017;7:884–99. https://doi.org/10.1158/2159-8290.CD-16-1297.
12. Lamonica JM, Deng W, Kadauke S, Campbell AE, Gamsjaeger R, Wang H, et al. Bromodomain protein Brd3 associates with acetylated GATA1 to promote its chromatin occupancy at erythroid target genes. Proc Natl Acad Sci U S A 2011;108:E159–68. https://doi.org/10.1073/pnas.1102140108.
13. Tontsch-Grunt U, Traexler PE, Baum A, Musa H, Marzin K, Wang S, et al. Therapeutic impact of BET inhibitor BI 894999 treatment: back-translation from the clinic. Br J Cancer 2022;127:577–86. https://doi.org/10.1038/s41416-022-01815-5.
14. Krivtsov AV, Evans K, Gadrey JY, Eschle BK, Hatton C, Uckelmann HJ, et al. A menin-MLL inhibitor induces specific chromatin changes and eradicates disease in models of MLL-rearranged leukemia. Cancer Cell 2019;36:660–73.e11. https://doi.org/10.1016/j.ccell.2019.11.001.
15. Kwon MC, Thuring JW, Querolle O, Dai X, Verhulst T, Pande V, et al. Preclinical efficacy of the potent, selective menin-KMT2A inhibitor JNJ-75276617 (bleximenib) in KMT2A- and NPM1-altered leukemias. Blood 2024;144:1206–20. https://doi.org/10.1182/blood.2023022480.
16. Pan J, Meyers RM, Michel BC, Mashtalir N, Sizemore AE, Wells JN, et al. Interrogation of mammalian protein complex structure, function, and membership using genome-scale fitness screens. Cell Syst 2018;6:555–68.e7. https://doi.org/10.1016/j.cels.2018.04.011.
17. Malone CF, Mabe NW, Forman AB, Alexe G, Engel KL, Chen Y-JC, et al. The KAT module of the SAGA complex maintains the oncogenic gene expression program in MYCN- amplified neuroblastoma. Sci Adv 2024;10:eadm9449. https://doi.org/10.1126/sciadv.adm9449.
18. Rzymski T, Mikula M, Żyłkiewicz E, Dreas A, Wiklik K, Gołas A, et al. SEL120-34A is a novel CDK8 inhibitor active in AML cells with high levels of serine phosphorylation of STAT1 and STAT5 transactivation domains. Oncotarget 2017;8:33779–95. https://doi.org/10.18632/oncotarget.16810.
19. Hatcher JM, Vatsan PS, Wang E, Jiang J, Gray NS. Development of highly potent and selective pyrazolopyridine inhibitor of CDK8/19. ACS Med Chem Lett 2021;12:1689–93. https://doi.org/10.1021/acsmedchemlett.1c00300.
20. Tsai KL, Sato S, Tomomori-Sato C, Conaway RC, Conaway JW, Asturias FJ. A conserved Mediator-CDK8 kinase module association regulates Mediator-RNA polymerase II interaction. Nat Struct Mol Biol 2013;20:611–9. https://doi.org/10.1038/nsmb.2549.
21. Zhang H, Chen DH, Mattoo RUH, Bushnell DA, Wang Y, Yuan C, et al. Mediator structure and conformation change. Mol Cell 2021;81:1781–8.e4. https://doi.org/10.1016/j.molcel.2021.01.022.
22. Tsai KL, Yu X, Gopalan S, Chao TC, Zhang Y, Florens L, et al. Mediator structure and rearrangements required for holoenzyme formation. Nature 2017;544:196–201. https://doi.org/10.1038/nature21393.
23. Chen M, Li J, Zhang L, Wang L, Cheng C, Ji H, et al. CDK8 and CDK19: positive regulators of signal-induced transcription and negative regulators of Mediator complex proteins. Nucleic Acids Res 2023;51:7288–313. https://doi.org/10.1093/nar/gkad538.
24. Firestein R, Bass AJ, Kim SY, Dunn IF, Silver SJ, Guney I, et al. CDK8 is a colorectal cancer oncogene that regulates beta-catenin activity. Nature 2008;455:547–51. https://doi.org/10.1038/nature07179.
25. Bancerek J, Poss ZC, Steinparzer I, Sedlyarov V, Pfaffenwimmer T, Mikulic I, et al. CDK8 kinase phosphorylates transcription factor STAT1 to selectively regulate the interferon response. Immunity 2013;38:250–62. https://doi.org/10.1016/j.immuni.2012.10.017.
26. Kwak H, Fuda NJ, Core LJ, Lis JT. Precise maps of RNA polymerase reveal how promoters direct initiation and pausing. Science 2013;339:950–3. https://doi.org/10.1126/science.1229386.
27. Mahat DB, Kwak H, Booth GT, Jonkers IH, Danko CG, Patel RK, et al. Base-pair-resolution genome-wide mapping of active RNA polymerases using precision nuclear run-on (PRO-seq). Nat Protoc 2016;11:1455–76. https://doi.org/10.1038/nprot.2016.086.
28. Wang J, Zhao Y, Zhou X, Hiebert SW, Liu Q, Shyr Y. Nascent RNA sequencing analysis provides insights into enhancer-mediated gene regulation. BMC Genomics 2018;19:633. https://doi.org/10.1186/s12864-018-5016-z.
29. Schiaffino S, Rossi AC, Smerdu V, Leinwand LA, Reggiani C. Developmental myosins: expression patterns and functional significance. Skelet Muscle 2015;5:22. https://doi.org/10.1186/s13395-015-0046-6.
30. Schiaffino S, Reggiani C. Fiber types in mammalian skeletal muscles. Physiol Rev 2011;91:1447–531. https://doi.org/10.1152/physrev.00031.2010.
31. Chargé SB, Rudnicki MA. Cellular and molecular regulation of muscle regeneration. Physiol Rev 2004;84:209–38. https://doi.org/10.1152/physrev.00019.2003.
32. Doench JG, Fusi N, Sullender M, Hegde M, Vaimberg EW, Donovan KF, et al. Optimized sgRNA design to maximize activity and minimize off-target effects of CRISPR-Cas9. Nat Biotechnol 2016;34:184–91. https://doi.org/10.1038/nbt.3437.
33. Bassi ZI, Fillmore MC, Miah AH, Chapman TD, Maller C, Roberts EJ, et al. Modulating PCAF/GCN5 immune cell function through a PROTAC approach. ACS Chem Biol 2018;13:2862–7. https://doi.org/10.1021/acschembio.8b00705.
34. Spitz F, Demignon J, Porteu A, Kahn A, Concordet JP, Daegelen D, et al. Expression of myogenin during embryogenesis is controlled by Six/sine oculis homeoproteins through a conserved MEF3 binding site. Proc Natl Acad Sci U S A 1998;95:14220–5. https://doi.org/10.1073/pnas.95.24.14220.

35. Niro C, Demignon J, Vincent S, Liu Y, Giordani J, Sgarioto N, et al. Six1 and Six4 gene expression is necessary to activate the fast-type muscle gene program in the mouse primary myotome. Dev Biol 2010;338:168–82. https://doi.org/10.1016/j.ydbio.2009.11.031.
36. Bernecky C, Grob P, Ebmeier CC, Nogales E, Taatjes DJ. Molecular architecture of the human Mediator-RNA polymerase II-TFIIF assembly. PLoS Biol 2011;9:e1000603. https://doi.org/10.1371/journal.pbio.1000603.
37. Liu Y, Ranish JA, Aebersold R, Hahn S. Yeast nuclear extract contains two major forms of RNA polymerase II mediator complexes. J Biol Chem 2001;276:7169–75. https://doi.org/10.1074/jbc.M009586200.
38. Paoletti AC, Parmely TJ, Tomomori-Sato C, Sato S, Zhu D, Conaway RC, et al. Quantitative proteomic analysis of distinct mammalian Mediator complexes using normalized spectral abundance factors. Proc Natl Acad Sci U S A 2006;103:18928–33. https://doi.org/10.1073/pnas.0606379103.
39. Myers LC, Gustafsson CM, Bushnell DA, Lui M, Erdjument-Bromage H, Tempst P, et al. The Med proteins of yeast and their function through the RNA polymerase II carboxy-terminal domain. Genes Dev 1998;12:45–54. https://doi.org/10.1101/gad.12.1.45.
40. Knuesel MT, Meyer KD, Bernecky C, Taatjes DJ. The human CDK8 subcomplex is a molecular switch that controls Mediator coactivator function. Genes Dev 2009;23:439–51. https://doi.org/10.1101/gad.1767009.
41. Tsai K-L, Tomomori-Sato C, Sato S, Conaway RC, Conaway JW, Asturias FJ. Subunit architecture and functional modular rearrangements of the transcriptional mediator complex. Cell 2014;157(6):1430–1444. https://doi.org/10.1016/j.cell.2014.05.015.
42. Akoulitchev S, Chuikov S, Reinberg D. TFIIH is negatively regulated by cdk8-containing mediator complexes. Nature 2000;407:102–6. https://doi.org/10.1038/35024111.
43. Lynch CJ, Bernad R, Martínez-Val A, Shahbazi MN, Nóbrega-Pereira S, Calvo I, et al. Global hyperactivation of enhancers stabilizes human and mouse naive pluripotency through inhibition of CDK8/19 Mediator kinases. Nat Cell Biol 2020;22:1223–38. https://doi.org/10.1038/s41556-020-0573-1.
44. Pelish HE, Liau BB, Nitulescu II, Tangpeerachaikul A, Poss ZC, Da Silva DH, et al. Mediator kinase inhibition further activates super-enhancer-associated genes in AML. Nature 2015;526:273–6. https://doi.org/10.1038/nature14904.
45. Lynch CJ, Bernad R, Calvo I, Serrano M. Manipulating the Mediator complex to induce naïve pluripotency. Exp Cell Res 2020;395:112215. https://doi.org/10.1016/j.yexcr.2020.112215.
46. Adler AS, McCleland ML, Truong T, Lau S, Modrusan Z, Soukup TM, et al. CDK8 maintains tumor dedifferentiation and embryonic stem cell pluripotency. Cancer Res 2012;72:2129–39. https://doi.org/10.1158/0008-5472.CAN-11-3886.
47. Lee JC, Liu S, Wang Y, Liang Y, Jablons DM. MK256 is a novel CDK8 inhibitor with potent antitumor activity in AML through downregulation of the STAT pathway. Oncotarget 2022;13:1217–36. https://doi.org/10.18632/oncotarget.28305.
48. Laubscher D, Gryder BE, Sunkel BD, Andresson T, Wachtel M, Das S, et al. BAF complexes drive proliferation and block myogenic differentiation in fusion-positive rhabdomyosarcoma. Nat Commun 2021;12:6924. https://doi.org/10.1038/s41467-021-27176-w.
49. Relaix F, Demignon J, Laclef C, Pujol J, Santolini M, Niro C, et al. Six homeoproteins directly activate Myod expression in the gene regulatory networks that control early myogenesis. PLoS Genet 2013;9:e1003425. https://doi.org/10.1371/journal.pgen.1003425.
50. Giordani J, Bajard L, Demignon J, Daubas P, Buckingham M, Maire P. Six proteins regulate the activation of Myf5 expression in embryonic mouse limbs. Proc Natl Acad Sci U S A 2007;104:11310–5. https://doi.org/10.1073/pnas.0611299104.
51. Hsu JY, Danis EP, Nance S, O'Brien JH, Gustafson AL, Wessells VM, et al. SIX1 reprograms myogenic transcription factors to maintain the rhabdomyosarcoma undifferentiated state. Cell Rep 2022;38:110323. https://doi.org/10.1016/j.celrep.2022.110323.
52. Spassov DS, Atanasova M, Doytchinova I. Inhibitor trapping in kinases. Int J Mol Sci 2024;25:3249. https://doi.org/10.3390/ijms25063249.
53. Hopkins TA, Shi Y, Rodriguez LE, Solomon LR, Donawho CK, DiGiammarino EL, et al. Mechanistic dissection of PARP1 trapping and the impact on in vivo tolerability and efficacy of PARP inhibitors. Mol Cancer Res 2015;13:1465–77. https://doi.org/10.1158/1541-7786.MCR-15-0191-T.
54. Rohle D, Popovici-Muller J, Palaskas N, Turcan S, Grommes C, Campos C, et al. An inhibitor of mutant IDH1 delays growth and promotes differentiation of glioma cells. Science 2013;340:626–30. https://doi.org/10.1126/science.1236062.
55. Issa GC, Aldoss I, DiPersio J, Cuglievan B, Stone R, Arellano M, et al. The menin inhibitor revumenib in KMT2A-rearranged or NPM1-mutant leukaemia. Nature 2023;615:920–4. https://doi.org/10.1038/s41586-023-05812-3.
56. Westerling T, Kuuluvainen E, Mäkelä TP. Cdk8 is essential for preimplantation mouse development. Mol Cell Biol 2007;27:6177–82. https://doi.org/10.1128/MCB.01302-06.
57. Loncle N, Boube M, Joulia L, Boschiero C, Werner M, Cribbs DL, et al. Distinct roles for Mediator Cdk8 module subunits in Drosophila development. EMBO J 2007;26:1045–54. https://doi.org/10.1038/sj.emboj.7601566.
58. Bruter AV, Varlamova EA, Stavskaya NI, Antysheva ZG, Manskikh VN, Tvorogova AV, et al. Knockout of cyclin-dependent kinases 8 and 19 leads to depletion of cyclin C and suppresses spermatogenesis and male fertility in mice. eLife 2025;13:RP96465. https://doi.org/10.7554/eLife.96465.4.
59. Koscielniak E, Stegmaier S, Ljungman G, Kazanowska B, Niggli F, Ladenstein R, et al. Prognostic factors in patients with localized and metastatic alveolar rhabdomyosarcoma. A report from two studies and two registries of the Cooperative Weichteilsarkom Studiengruppe CWS. Cancer Med 2025;14:e70215. https://doi.org/10.1002/cam4.70215.
60. Stewart E, Federico SM, Chen X, Shelat AA, Bradley C, Gordon B, et al. Orthotopic patient-derived xenografts of paediatric solid tumours. Nature 2017;549:96–100. https://doi.org/10.1038/nature23647.
61. Mimoso CA, Goldman SR. PRO-seq: precise mapping of engaged RNA Pol II at single-nucleotide resolution. Curr Protoc 2023;3:e961. https://doi.org/10.1002/cpz1.961.
62. Ritchie ME, Phipson B, Wu D, Hu Y, Law CW, Shi W, et al. limma powers differential expression analyses for RNA-sequencing and microarray studies. Nucleic Acids Res 2015;43:e47. https://doi.org/10.1093/nar/gkv007.
63. Tsitsiridis G, Steinkamp R, Giurgiu M, Brauner B, Fobo G, Frishman G, et al. CORUM: the comprehensive resource of mammalian protein complexes-2022. Nucleic Acids Res 2023;51:D539–45. https://doi.org/10.1093/nar/gkac1015.
64. Steinkamp R, Tsitsiridis G, Brauner B, Montrone C, Fobo G, Frishman G, et al. CORUM in 2024: protein complexes as drug targets. Nucleic Acids Res 2025;53:D651–7. https://doi.org/10.1093/nar/gkae1033.
65. Anders S, Huber W. Differential expression analysis for sequence count data. Genome Biol 2010;11:R106. https://doi.org/10.1186/gb-2010-11-10-r106.
66. Skene PJ, Henikoff JG, Henikoff S. Targeted in situ genome-wide profiling with high efficiency for low cell numbers. Nat Protoc 2018;13:1006–19. https://doi.org/10.1038/nprot.2018.015.